Superconductor Science and Technology

PAPER • **OPEN ACCESS**

On the mechanics of MQXFB—the low-beta quadrupole for the HL-LHC

To cite this article: E Takala *et al* 2021 *Supercond. Sci. Technol.* **34** 095002

View the article online for updates and enhancements.

IOP ebooks™

Bringing together innovative digital publishing with leading authors from the global scientific community.

Start exploring the collection–download the first chapter of every title for free.

This content was downloaded from IP address 128.141.192.28 on 18/08/2021 at 14:58

OPEN ACCESS
IOP Publishing
Superconductor Science and Technology
Supercond. Sci. Technol. **34** (2021) 095002 (20pp)
https://doi.org/10.1088/1361-6668/ac1526

On the mechanics of MQXFB—the low-beta quadrupole for the HL-LHC

E Takala[1,*], L Bianchi[1], F Lackner[1], P Ferracin[2], S Izquierdo Bermudez[1] and D Pulikowski[1]

[1] Technology Department, CERN, Geneva, Switzerland
[2] Berkeley Center for Magnet Technology, Lawrence Berkeley National Lab, Berkeley, United States of America

E-mail: eelis.takala@gmail.com

Received 4 March 2021, revised 30 June 2021
Accepted for publication 16 July 2021
Published 4 August 2021

Abstract

The High Luminosity Large Hadron Collider (LHC) Project target is to reach an integrated luminosity of the LHC of 3000 fb^{-1}, corresponding to a factor 10 increase in collisions with respect to the current accelerator. One of the main components is the superconducting quadrupole called MQXF. It is based on Nb_3Sn technology and has a 150 mm single aperture with a field gradient of 132.6 T m^{-1}. The MQXF magnets are currently in preseries production in a joint collaboration between CERN and the US-LHC Accelerator Upgrade Project. The first prototype magnet based on 7 m-long coils (MQXFBP1) was assembled and preloaded in 2019. The testing and disassembly was done in 2020. The coils were equipped with optical fiber Bragg grating (FBG) sensors. Some of the FBG values exhibited strain jumps during preload and their signals were lost during cool-down. The magnet did not reach the nominal current, quenching at 15.15 kA. At the time of writing three MQXFB magnets have been preloaded from which the second prototype is soon to be tested. The objective of this paper is to analyze the mechanical behavior of MQXFB magnets in the light of current knowledge, thanks to earlier short model experiments, as well as describe in detail the process of assembly and preload. We synthesize the mechanical theory of preload and present new considerations on symmetric/asymmetric bladder-key operations and their effects. An extensive comparison between long and short model magnets is presented. In our analysis and FE modeling we take into account the measured coil sizes that vary over position. We introduce a novel technique that allows preload homogenization over the length of the magnet after preload has been done. We analyze the role of the stainless steel shell and show its mechanical behavior. Finally, the relevant data at cold is presented and analyzed.

Keywords: high Large Hadron Collider (LHC), low-β quadrupoles, Nb_3Sn magnets, long prototype, support structure

(Some figures may appear in colour only in the online journal)

1. Introduction

The HI-Lumi project aims to improve the luminosity of the Large Hadron Collider (LHC) by a factor of ten [1]. One of the main components in this project is the so called inner triplet that consists of MQXF [2–6] superconducting Nb_3Sn low-β quadrupole magnets. There are MQXFA and MQXFB variants that are mainly different in length (4.2 and 7.5 m, respectively). The MQXFA is produced by the US Accelerator Upgrade Project (AUP, the continuation of LARP [7]) and MQXFB is produced by CERN.

MQXFA has seen two successful full length magnet prototypes MQXFAP1 and MQXFAP2 [8]. The first prototype

* Author to whom any correspondence should be addressed.

 © 2021 The Authors. Published by IOP Publishing Ltd Printed in the UK

This is an open access article distributed under the terms of the Creative Commons Attribution 4.0 License.
Any further distribution of this work must maintain attribution to the author(s) and the title of the work, journal citation and DOI.

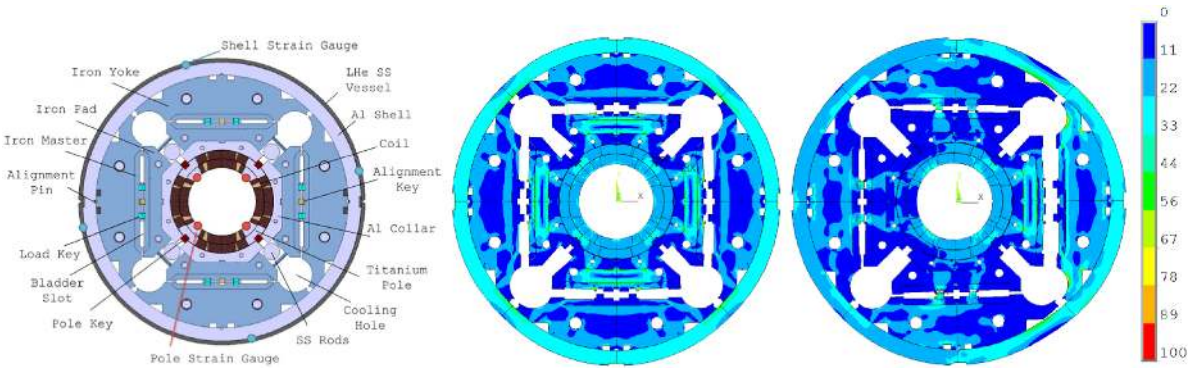

Figure 1. From left to right: the first image shows the mechanical features of the MQXF magnet, the second shows an FEM (finite element model) result in which all of the bladders are pressurized and the third shows an FEM result in which only the bladders in the right quadrant are pressurized. Typically, these two bladder-key operation types are considered, as the keys can be changed in all quadrants at the same time or one quadrant at a time. Here, the FEM assumes a 13.1 mm key (100 μm interference) inserted in all slots and the bladders are pressurized until 100 bars. The displacement is scaled by a factor of 50 and the color map shows the von Mises stress from 0 to 100 MPa. The FEM model is a full 2D model introduced in detail in [10].

was rebuilt and tested as MQXFAP1b. Each of the magnets revealed a specific issue that was addressed or is under investigation [9].

At the time of writing, the MQXFB has seen two mechanical tests and a prototype, called MQXFBP1. The second prototype and the first preseries magnets, called MQXFBP2 and MQXFB01, respectively, have been preloaded but not tested yet. The second preseries magnet, called MQXFB02, is planned to be assembled. The second mechanical test, called MQXFBMT2, was conducted before the assembly of MQXFBP2 in order to gain experience and knowledge of the practical aspects of a long prototype magnet.

In this paper we discuss the mechanics of MQXF in general and report about the MQXFB mechanical development in the light of the theory and understanding developed over the years, thanks to short model (MQXFS) experiments. Due to the lack of cold test data, we focus specifically on the preload. In section 2 we present briefly the mechanical design of MQXF and the strain instrumentation installed in short models and prototypes. In section 3 we show, in detail, the structure and assembly procedure of the coil pack that plays a crucial role in the mechanics of the magnet. We focus on the coil metrology measurements and their important role on the preload characteristics. In section 4 we present the preload procedure and we focus, in particular, to the bladder operations. In section 5 we give important notes on the coil strain measurements in MQXFBP1 that exhibited unexpected behavior and in section 6 we present an extensive description of the loading mechanics theory that takes into account the real coil sizes. Moreover, we introduce a new technique, called the variable load key, for homogenizing the preload along the length that may be different due to different coil sizes and we expand the notion of the, so called, Long Quadrupole (LQ) effect [11, 12]. We compare and discuss the results of long prototypes and short models. In section 7 we discuss the role of the stainless steel shell. In section 8 we report the relevant cold test results, summarize in section 9 and conclude in section 10.

2. The instrumentation and mechanical design of MQXF

From the mechanical point of view, a common paradigm in the design of accelerator magnets is to minimize coil movement caused by electromagnetic forces acting on the coils during powering. The forces are such that on one hand they work for detaching the coil from the pole and for pressing it toward the mid-plane (MP) [13] and on the other hand they work for pulling on the coil heads [14]. A typical approach is to apply counter forces via preload, equal but opposite to the nominal electromagnetic force. In theory, coil movement may cause local disturbance in the superconductor and trigger a normal zone leading, possibly, to a quench [15]. In fact, it has been shown that allowing movement by lowering the level of preload leads to longer training and lower quench current in MQXF [10, 16]. The preload is applied before the magnet is at cold and ready to be operated.

The preload is typically broken down into azimuthal and longitudinal components. The azimuthal preload in MQXF relies on the so called bladder-key technology [17]. When the bladders are pressurized in their slots (figure 1) the masters tend to separate creating more space in between them and in the load key slots. The displacement causes azimuthal tension in the aluminum shell and compression in the coils. Load keys are then inserted in the key slots for locking down the masters to their positions in order to conserve the displacement and the resulting azimuthal preload. The bladders can then be removed from their slots.

In MQXFB, the shell and coils are equipped with strain sensors (figure 1) at lead end (LE), center end (CE) and return end (RE) (figure 2) as there can be longitudinal variation in a long structure. The shells are equipped with electrical strain gauges. In the short model magnets, called MQXFS, both the electrical and modern optical sensors (fiber Bragg grating, FBG) were tested on the pole. The optical sensors are generally considered robust and require less space [18]. In fact, MQXFB magnets need to be equipped with the FBG gauges

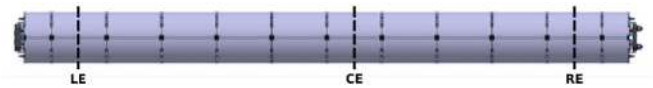

Figure 2. MQXFB side view showing the three longitudinal locations (LE, CE and RE) where the strain sensors are installed. The image shows only the segmented aluminum shell (the stainless steel shell is excluded w.r.t. figure 1).

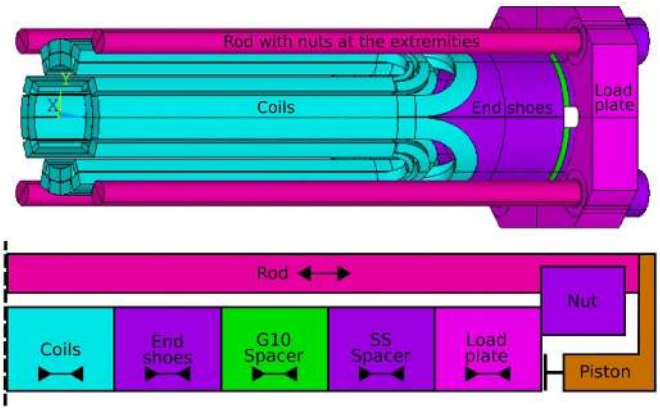

Figure 3. A geometrical 3D representation and a topological representation of the head of the longitudinal loading system of MQXF on top and bottom images, respectively.

due to the lack of space when the so called cold bore tube is installed in the magnet bore. The electrical gauges can be used in the aluminum shell to monitor the strain until the end of the preload process. Then they have to be removed due to the outer stainless steel shell (LHe SS Vessel, figure 1) that is installed in contact with the aluminum shell. In MQXFBP1, the stainless steel shell was equipped with electrical strain gauges.

The longitudinal preload relies on rods that are in parallel with the structure and attached to the load plates at both ends (figure 3). The load plates are connected to the coil ends via spacers and provide the longitudinal support. The preload is exerted with a piston that pushes against the plate and pulls on the rods. When the target preload is reached the rod nuts are tightened to lock the rod to the plate so that the longitudinal stress is conserved. The piston is then removed. The electromagnetic pull force at the head of the coil is the same in short and long magnets, thus, the stiffness of the longitudinal loading system needs to match also. However, the stiffness decreases linearly as a function of length. Therefore, the rods in short and long magnets are made of aluminum and stainless steel, respectively [14].

When the magnet is cooled down the stainless steel rods and aluminum shell shrink more than the coils and rest of the structure due to higher coefficients of thermal contraction. Thus, part of the prestress is gained during the cool-down.

3. The coil pack sub-assembly

3.1. The coil pack

The effort of applying the prestress requires a well designed assembly procedure as well as a stiff and conform coil to

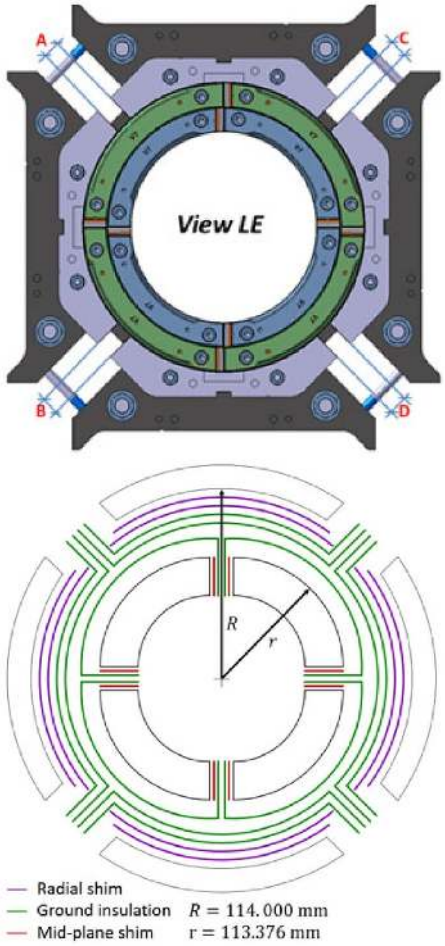

Figure 4. The coil pack sub-assembly of MQXF showing the collar gaps (A), (B), (C), (D) and a schematic view of the nominal shimming plan showing the relationship between collars and coils.

structure interfaces in order to ensure the mechanical integrity of the coil. Therefore, the coil pack sub-assembly that consists of coils, collars and iron pads (see figure 4) is a very important aspect of a successful MQXF magnet. In this work, coil pack refers to the sub-assembly without iron pads or collars. The iron pads (together with iron masters) are used to transfer compression from the key and bladder slots to the collars.

In the assembly phase, the pads are tightened using the row of bolts at the four corners along the length of the structure while monitoring the coil strain gauges. The objective is not to simulate the loading, but to hold the assembly together with local contact pressure less than 10 MPa. The observed pole strains are usually in the order of 10 μe. In theory, the pole should go under compression azimuthally and under tension longitudinally, however, sometimes the reverse can happen if the coil to collar interface is non-conform, for example if the coil is too large so that the collar is in contact only on the pole (imagine only the extremities of the collars pushing against the poles; covered in section 6.7).

The bolting procedure is repeated at least two times: (1) FUJI film assembly and (2) final assembly. In the former, the contact in between the coil and collar is probed using a 170 μm

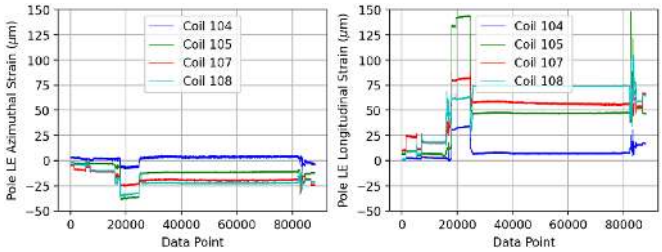

Figure 5. The azimuthal and longitudinal strain at the LE of MQXFBP1 during the FUJI assembly test.

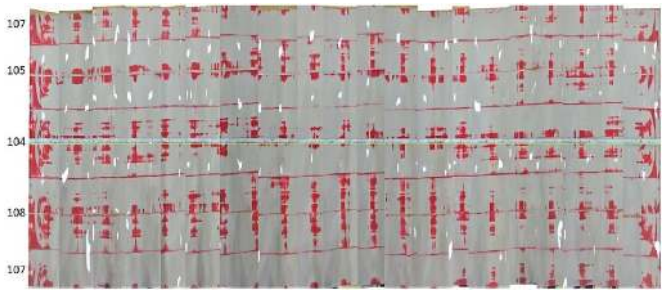

Figure 6. The FUJI film after the coil pack test assembly of MQXFBP1. The numbers on left hand side are the coil numbers. The pole of the coils are at the vertical positions of the numbers.

pressure sensitive FUJI film (low pressure, 2.5–10 MPa) instead of mere polyimide film at the coil to collar interface. If the contact is not adequate then the shimming can be adjusted and the FUJI procedure is repeated. The final assembly is done using the shimming that is found to best conform the coil to collar interface. However, the strain signals are very weak and usually no decisive conclusions can be made. In MQXFBP1, the effect on strain was less than 20 μe at the CE and RE showing no clear signs of non-conform interfaces. In the LE, the strain signal was stronger but did not indicate the reversed strain effect, see figure 5.

Figure 6 shows a typical (MQXFBP1) contact imprint on the film of FUJI assembly. The film shows that the contact pressure is the highest at the bolt locations, as expected. The pole is in good contact throughout the contact surface and in some parts of the coils, toward the MP, contact is less represented on the film. This could be an indication of incompatible curvatures of the coil and collar surfaces, e.g. the coil pack being too big. The FUJI assembly is not repeated in any of the MQXFB magnets so far: based on the short model experience the contact seems adequate.

3.2. Shimming plan

In the nominal design of MQXF, 625 μm is left in between the coils and collars as well as 250 μm in between the coil MPs. This space is then shimmed for a tight fitting as follows (figure 4): the outer surface of each of the four coils is covered with a layer of 125 μm polyimide film ground insulation (GI) plied onto the sides (MPs). The insulated coils are used in order to assemble a coil cylinder. Two additional layers of GI, each consisting of four collar matching parts, are

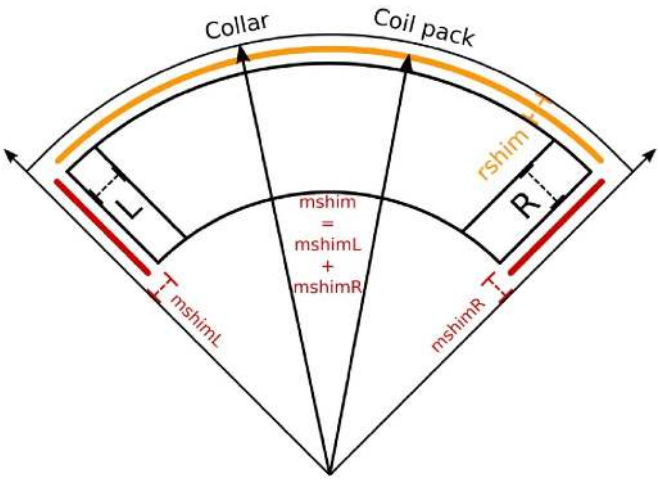

Figure 7. The shimming effect in the coil pack of MQXFB. L and R are the measured left and right coil excess', respectively, mshim is the total MP shim including left and right sides of the coil. The values are deviations from the nominal values. For example, rshim is zero if the total radial shimming between coil and collar is 625 μm and mshim is zero if the MP contains only the GI layers. The definition of coil pack includes all the shimming.

added on top. The matching parts are plied outwards in the collar gap. The purpose of the GI is to avoid contact between the different parts (coil-coil, coil-collar and collar-pole). In the nominal case, two additional shimming layers of 125 μm polyimide film are added on top of the GI. Thus, the nominal total radial shimming in between coil and collar is 625 μm. The additional layers can be removed completely or replaced with shims of different thickness or number. These layers can be used to adjust the fitting of the collars and the insulated coil cylinder that may deviate from the nominal size. Historically, there is a convention of removing 125 μm compared to the theoretical radial shimming in order to improve the coil to collar interface (explained in detail in section 6.7). In MQXFBP1 the additional layers are removed so that the total radial shimming is 375 μm (or −250 μm w.r.t. nominal).

The resulting coil pack is almost always different compared to the design as the coils do not exactly respect their nominal dimensions. In a rigid system, even small variations of dimension can cause considerable stress distribution deviations [10]. Moreover, the conductors get misplaced which may compromise the field quality of the magnet. In order to minimize the stress deviations caused by the azimuthal size variations in the coils, conventionally, some mechanical optimization has been made by adding filling material to the individual coils (MP shims). In MQXFB, the coils are shimmed to the measured dimensions of the largest coil in terms of azimuthal size. On a practical note, the coil shims can be chosen in 50 μm increments (25 μm/side). This leads to some approximation errors in the final product.

Increasing the radial or MP shimming increases the coil pack radial size (figure 7) that w.r.t. nominal can be computed as

$$\Delta R_{\mathrm{coilpack}} = 2(\mathrm{L} + \mathrm{R} + \mathrm{mshim})/\pi + \mathrm{rshim} \qquad (1)$$

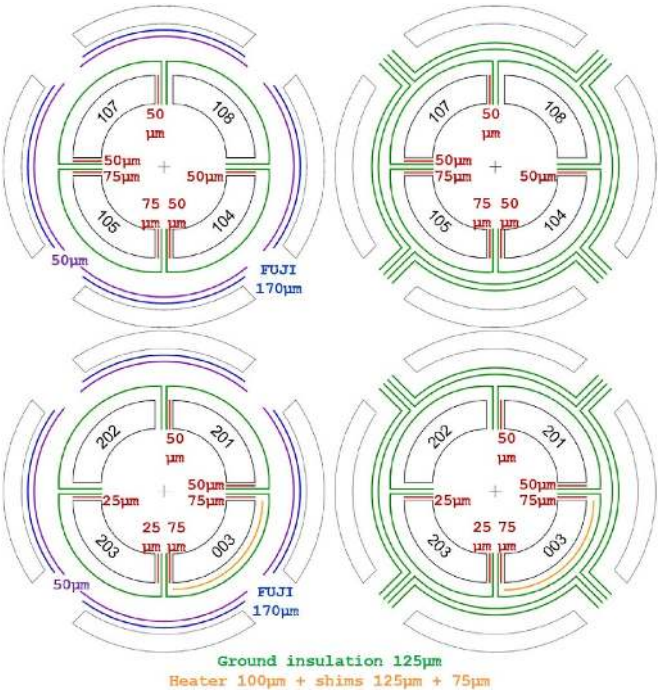

Figure 8. From left to right column: the FUJI test and final assembly shimming plans. Top to bottom: MQXFBP1 and MQXFBMT2. Coil 003 was a test, made 200 μm smaller radially in order to fit the external quench heater.

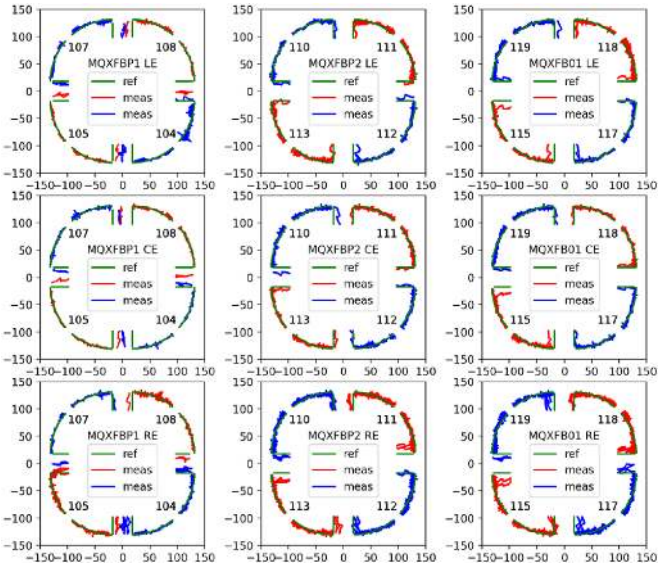

Figure 9. The coil metrology results at each longitudinal location (from top to bottom: LE, CE and RE) where the strain gauges are located for MQXFBP1, MQXFBP2 and MQXFB01 from left and right columns, respectively. The green line ('ref') represents the nominal reference shape of the coil. The blue and red lines ('meas') represent the measured coil shape. The unit is mm and the deviation of measurements from the reference shape ('ref' to 'meas' distance) is scaled with a factor of 100 (1 unit = 10 μm). Notice the over sized MPs in MQXFBP1.

where R_{coilpack} is the coil pack radial size, L and R are the coil azimuthal excess on the left and right sides of the coil, respectively, mshim is the MP shimming thickness (including both sides) and rshim is the radial shimming thickness. The first term is simply the shimmed coil size converted from circumferential length to radial size. The mshim is always distributed symmetrically to the left and right sides of the coil. The down side is that if $\mathrm{L} \neq \mathrm{R}$ then the pole key, that is in the middle of the coil (figure 1), is asymmetrically positioned closer to one than to the other MP. This can cause one-sided pole key to collar contact in a loaded condition. However, in practice, the contact hasn't had a significant effect on the coil stress [10].

The plans are referred to as their rshim value. Figure 8 shows examples of a conventional shimming plan and a plan with an external heater installation (tested in MQXFBMT2). In the case of MQXFBP1 there are -280 μm FUJI and -250 μm final plans. The average coil size deviations $(\mathrm{L}+\mathrm{R})$ over the length are 185, 164, 234 and 297 μm (coils 104, 105, 107 and 108, respectively), the average $\mathrm{L}+\mathrm{R}$ being thus 220 μm. The average MP shim is 88 μm that for a -280 and -250 μm shimming plans yields -84 and -54 μm coil pack sizes on average, respectively. The FUJI plan has a small deviation from the final plan as the FUJI film thickness does not match with the linear combination of available polyimide film layer thicknesses.

The coil order permutation can be determined by choosing the least compromised in terms of field quality or developed voltage during a quench. The field quality is computed in 2D ROXIE [19] model taking into account the $\mathrm{L}+\mathrm{R}$ of the coils and their shimming. The developed voltage can be computed in LEDET [20]. In MQXFBP1 the field quality was optimized, however in later assemblies the quench voltage minimization is preferred.

3.3. Coil sizes

The metrology measurements [21] are conducted for each individual coil using a FaroArm in order to determine the azimuthal excess. The cross-section of the coils are measured every 200 mm in the straight section from 400 to 7200 mm measured from the LE of the coil and every 50 mm at the ends. The data is aligned against a reference shape radially with the outer radius and azimuthally with the pole key slot over the length. Figure 9 shows metrology results of the coils of MQXFBP1, MQXFBP2 and MQXFB01 in their mechanical frame of reference at each of the three longitudinal locations where the strain state of the magnet over the cross-section is measured at four different locations on the shell and pole.

The coil azimuthal excess is computed for each of the measured cross-sections. The excess, shimmed excess and the theoretical load key of MQXFB magnets are shown in figure 10. The azimuthal excess shows that the coil sizes can vary not only among coils but along the length as well. So far, the center is always larger than the ends. Test coil 003 is one exception where the size is more uniform. This coil was produced with a different radial size due to an external heater installation that would have otherwise added the total radial size by 200 μm (figure 8). The different molding procedure could explain the difference in the shape over the length. In the first magnet,

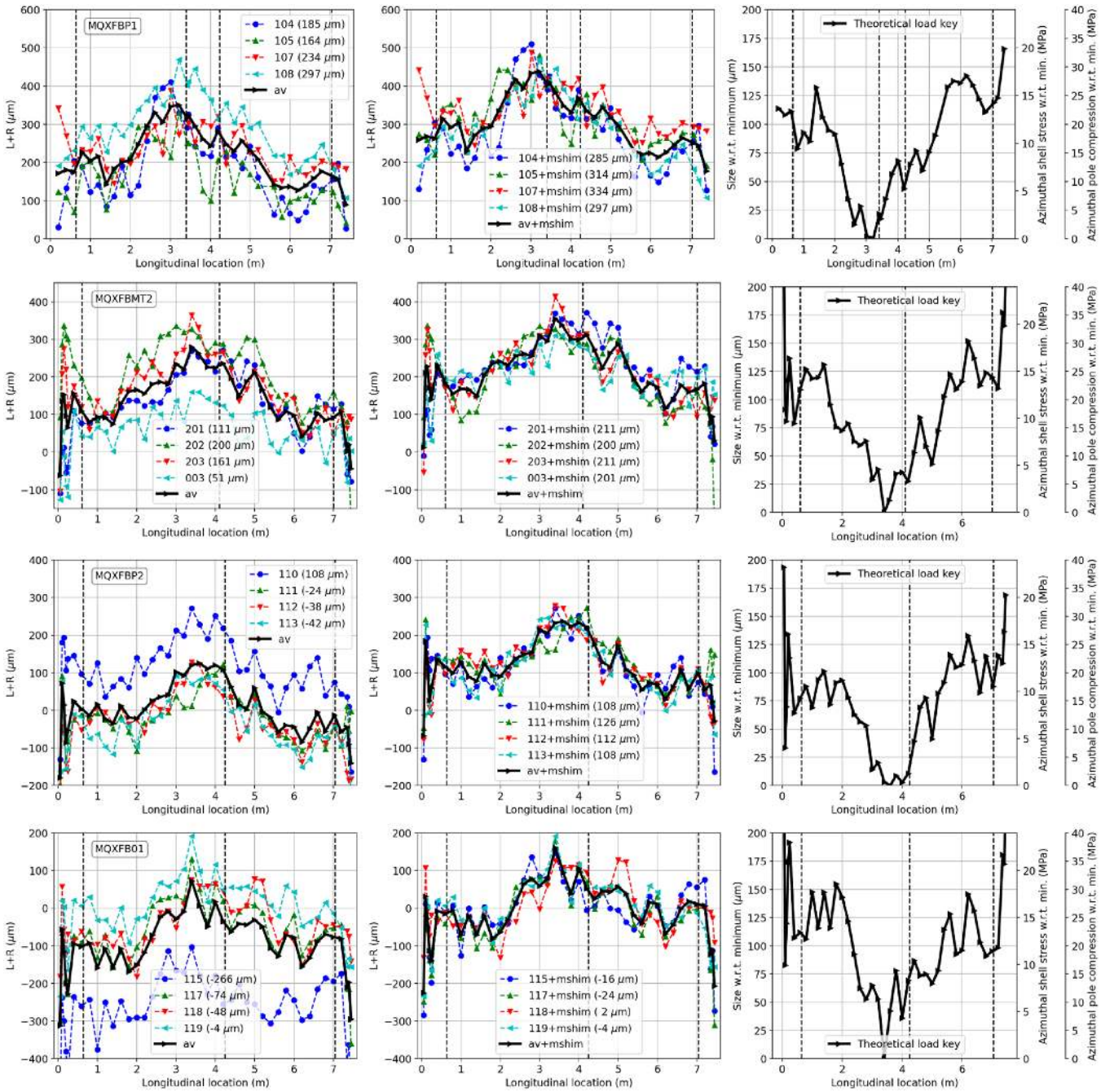

Figure 10. Columns from left to right: coil azimuthal excess, shimmed coil azimuthal excess and the theoretical load key as a function of longitudinal position. The magnets are arranged in chronological order from top to bottom row: MQXFBP1, MQXFBMT2, MQXFBP2 and MQXFB01. The legend shows the coil number and in brackets its average azimuthal excess over the length. The vertical dashed lines mark the longitudinal locations of strain sensors along the length. MQXFBP1 shell gauges were accidentally installed to different longitudinal locations: the first and second central lines represent the shell and pole sensors, respectively.

MQXFBP1, the LE side is clearly bigger than the RE side and the peak size tends toward the LE. In the successors the shape is more symmetric over the length. The shimmed excess shows how the MP shim narrows the effective assembled size of the coils. The theoretical load key represents a load key of a variable size that assures a constant azimuthal preload. In the plots, the size variation and the induced azimuthal stress variation w.r.t. the smallest value of such a key, based on the coil pack sizes, are presented. The coil size variation affects on the level of preload that can be corrected with the theoretical load key. The origins, testing and detailed analysis are presented in sections 6.3 and 6.4.

4. The preload procedure

The coil pack sub-assembly is installed inside the shell-yoke module together with the other parts of the structure. The coil

pack is free to move, as in theory the closest distance between the masters is 3 mm. Before the actual loading is started, it is important to verify that the coil pack is in good contact and centered w.r.t. the structure as accurately as possible. This operation is called centering and it is done by inserting the initial set of keys. The nominal key that engages the parts in contact without any interference is 13 mm. The available key sizes range from 13.0 to 14.0 mm with steps of 200 μm (custom key sizes can be manufactured if needed). Based on the short models and the coil pack sizes, 13.2 mm is chosen as the centering key thickness.

For inserting the centering key, some force is required in order to fit the keys in. Thus, the bladder-key operation needs to be used already in the centering phase. There are two main options for a bladder-key operation: (1) the full operation (F) and (2) the quadrant-by-quadrant operation (Q); see figure 1. In F, the bladder operation is done in all of the quadrants at the same time. The bladders are connected in parallel to the same pressure, exerting equal and symmetric force to the structure. It is thus expected that this operation conserves the state of symmetry (in particular, asymmetric stays asymmetric). In Q, the bladder operation is done one quadrant at the time. When only the bladders on one side of the coil pack are pressurized, the exerted force is asymmetric. It is thus expected that the Q operation is symmetry breaking, in particular, the coil pack should move toward the opposite side of the operated bladders. This can be used to fix some asymmetric (off centered) positions.

One major difference in F and Q operations is the required pressure increment for further opening up the key slots. Figure 11 shows the pressure requirement for a given key size in MQXFS6b, MQXFBP1 and different FEM cases. The FEM cases are computed using the full 2D model (see figure 1). As opposed to a mixed state, the cases assume an initial full loading state where all the load keys are of the same size [12]. The FEM shows that the pressure requirement for increasing the key slot using the F operation is linear with a slope of $k_F = 500$ bars mm^{-1}. The Q cases show that in order to increase the key slot, first the pressure has to be increased until the bladder pressure is enough to exert a force equal to that exerted by the key in the initial state. Let us call it the threshold pressure

$$P_{th} = k_F t_{if}, \tag{2}$$

where t_{if} is the key interference. Only pressure increments above the threshold adds work in to the system by increasing the key slot size. This means that the Q and F operations require equal pressures until the point where the slot starts to open. Until this point, mechanical work has not been done; only the role of the key is replaced by the pressurized bladder. From thereon, in theory, the slope of Q operation is $k_Q = 1/4\, k_F$ (125 bars mm^{-1}). However, the FEM cases show that it varies around 150 to 200 bars mm^{-1}; lower in cases with smaller and higher in cases with thicker initial key. This could be due to bending that makes the bladder operation less effective. Based on the FEM, the Q operation is beneficial only in further opening up the key slot. In fact, the key slot needs to be opened slightly more than the key size requires in order to

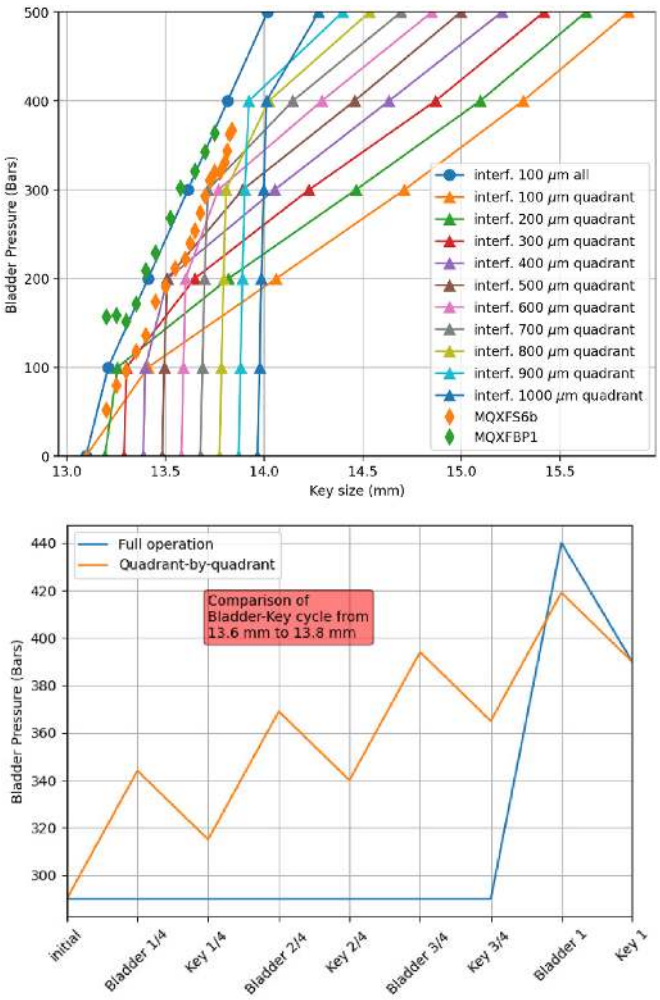

Figure 11. Top plot: the MQXF F (all) and Q (quadrant) operations bladder pressure requirement vs key size. Bottom plot: bladder-key cycle comparison from 13.6 to 13.8 mm key size.

freely slide the keys in. Thus, the minimum pressure needed for changing a key is

$$P_{ch,O} = P_{th} + k_O(\Delta t_{if} + t_{clr}), \tag{3}$$

where O is either Q or F, and t_{clr} is the additional clearance.

As an example, let us compare the F and Q operations when increasing the key size from 13.6 to 13.8 mm (figure 11). At 13.6 mm the threshold pressure is 290 bars. In the F operation, all the key slots are increased at the same time by 300 μm (100 μm extra clearance for sliding the key). Thus, 150 bars in addition to the threshold is needed (440 bars). In the Q operation, assuming a 180 bars mm^{-1} slope, the first operation requires 344 bars (+54 bars) in order to change the first key (300 μm opening). The threshold increases to 315 bars (+25 bars). When changing the last key, the threshold is 365 bars. Thus, the maximum pressure is 419 bars that is 21 bars less than in the full operation. If more clearance is needed, the difference in required pressure increases 320 bars mm^{-1}. The need for clearance may arise, for example, from mechanical imbalance. Such a case, could be an off-centered position. Not only the F operation need more clearance but it also

does not correct the asymmetry (being symmetry conserving). If the bladders in off-centered situation are Q operated from the looser side, the key fits more easily than in a centered situation. If they are Q operated from the tighter side, the imbalance is naturally corrected.

The Q operation has been used for all the MQXF magnets so far loaded at CERN As an example, the MQXFS6b and MQXFBP1 are shown in figure 11. They follow more or less the F operation curve, as expected. The pumping is stopped when the keys feel loose enough for fitting the next key. Thus, the data depends on the judgment of the technician. However, one can see that the MQXFS6b and MQXFBP1 curves are shifted w.r.t. each other that could be an indication of the larger coil pack size in MQXFBP1 (w.r.t. nominal at center: −40 vs −340 μm).

5. Notes on MQXFBP1 coil strain measurements

During the preload of MQXFBP1, the FBG strain values exhibited large jumps that could not be explained. In order to analyze the coil behavior, it was mandatory to understand if the jumps were physical or not. Thus, MQXFBMT2 was equipped with FBGs and SGs. The preload experiment showed that the FBG readings may exhibit artificial jumps that are not detected by SGs in the vicinity of the FBG measurement location: figure 12 shows FBG vs SG azimuthal strain comparison during the loading of MQXFBMT2. Thus, the MQXFBP1 FBG readings may also be affected by this unknown phenomenon.

During the cool down, the FBG signals were lost. This is most likely due to a fiber misalignment in the ultra high vacuum feedthrough connector [18]. The effect is under investigation. The FBG signals were recovered when the magnet was warmed up. The cool down and warm up was done a second time with a similar effect of loosing the FBG readings during cool down and recovering them at warm.

A detailed analysis of the strain measurement techniques used in MQXFBP1 is presented in [18]. Even though there are some pressing unanswered questions about the behavior of FBG sensors, there are very consistent individual readings between the results of different warm ups. This means that when behaving correctly, the FBG sensors can give consistent results throughout the lifetime of a magnet [10, 12]. Moreover, the MQXFBMT2 test demonstrates that even if the aforementioned jumping effect takes place in an FBG reading, the strain sensitivity is more or less the same before and after the jump. Thus, if the temporal location of the jumps are known their effect can be taken into account. This strategy was adopted in MQXFB strain analysis.

6. The loading mechanics of MQXF

6.1. The preload characterization

Figure 13 shows the transfer function—key plots (TF-KP) for MQXFBP1, MQXFBP2 and MQXFB01 for each longitudinal section together with the full FE model predictions [10] using the real coil sizes (figure 9). Table 1 shows the

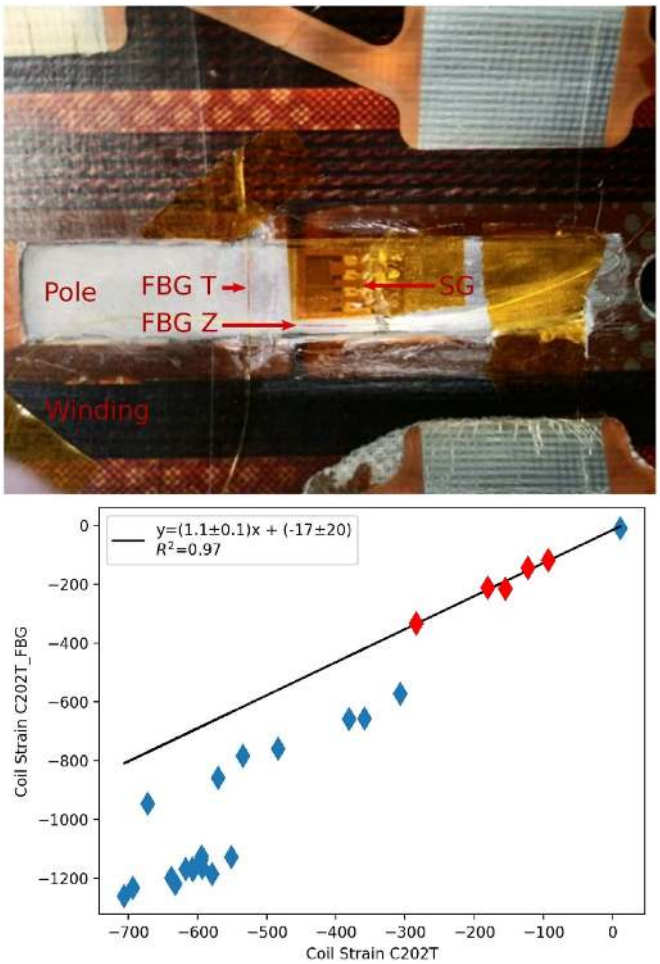

Figure 12. Top image: an example of SG and FBG installation on the inner pole surface of a coil. FBG active zone is the 5 mm long part of the fiber that is marked with red color. Bottom plot: FBG azimuthal strain vs SG azimuthal strain during MQXFBMT2 loading. The linear fit is done through the red points. The FBG readings have constant shifts w.r.t. SG, however the sensitivity remains similar (close to 1:1).

preload characterization [12] for MQXFB and MQXFS magnets. The meaning of the plots and parameters are explained in this section. MQXFBP2 was preloaded in two parts. The first part was done up to 13.6 mm key and the second part up to 13.8 mm. The second part is noted with suffix: for example, 'MQXFBP2 RE 2' means the second part of MQXFBP2 RE loading.

6.2. Key plots

In figure 14 one can see a close geometrical view of the first quadrant as well as a topological illustration of the collar and the pole key gaps. The pole key is attached to the pole key slot on the outer surface of the pole. The purpose of the key is to ensure the correct coil pack alignment w.r.t. the collar. Figure 15 upper image row shows the topology of MQXF in three cases from the azimuthal preload point of view: (1) pole key case where the coil pack and the pole key are in contact with the collars, (2) no pole key case where the pole key does

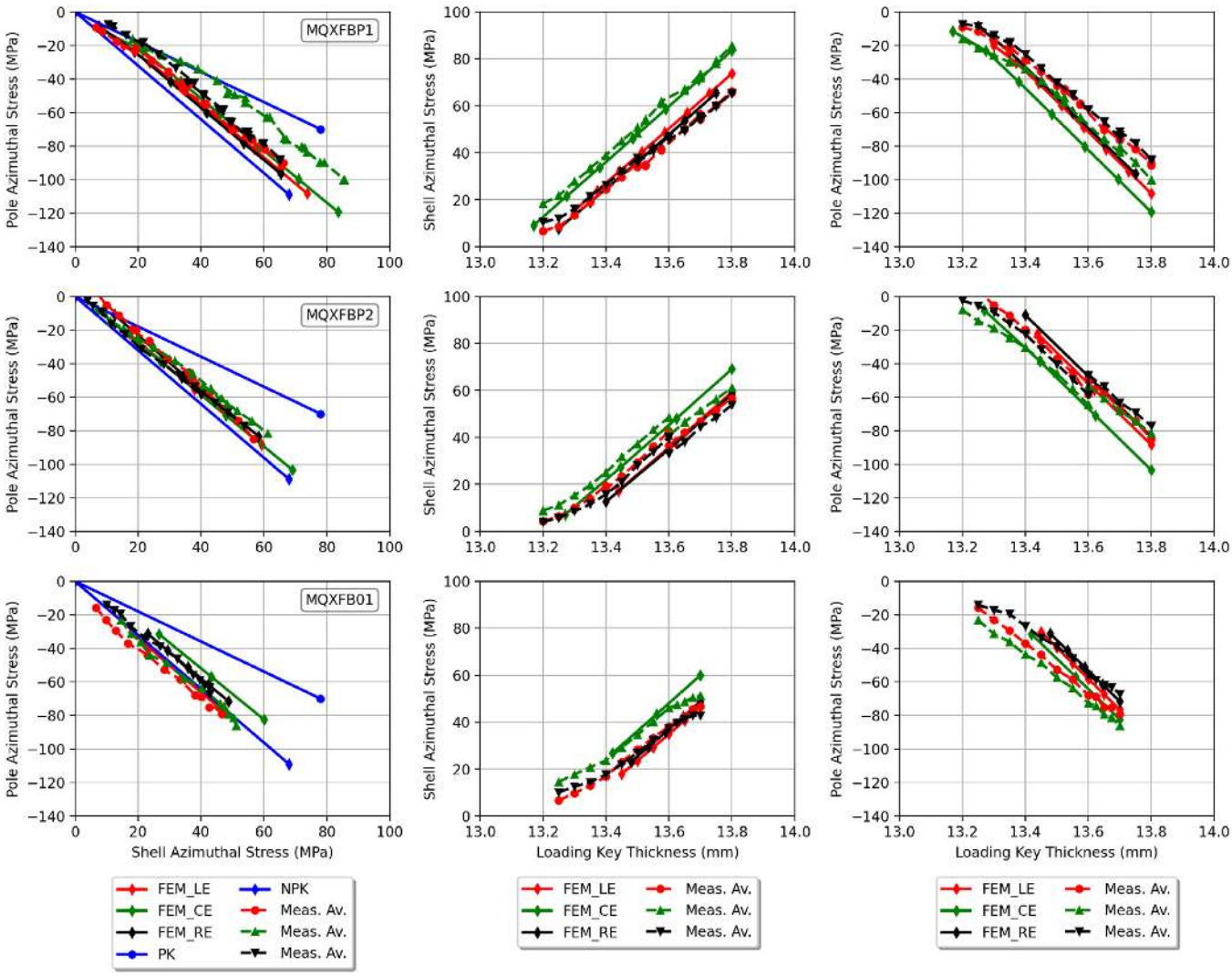

Figure 13. The image columns from left to right: transfer function, shell key plot and pole key plot. The rows from top to bottom are MQXFBP1, MQXFBP2 and MQXFB01. The red, green and black colors represent LE, CE and RE; respectively. Diamonds represent the full FE model predictions using the measured coil sizes (figure 9). Circles, upward triangles and downward triangles represent the LE, CE and RE measured values. The shell/pole keyplot represents shell/pole stress as a function of load key size and the transfer function represents the pole stress as a function of shell stress. Blue NPK and PK curves represent the so called no pole key and pole key lines. The FE model assumes 100 μm smaller structure than nominal due to short model experience [10].

not touch the collar and (3) large pole key case where the key is in contact with the collars before the coil to collar contact. The bottom row of figure 15 shows a schematic view of the key plots (load key size vs azimuthal stress) [12] in the three cases. In a key plot, there are two regimes: (1) the loose regime where the load key is small and there is no contact between the coil pack sub-assembly and the structure, (2) the contact regime, where further key increments lead to iron pads compressing the pole through the collars and iron yoke tensioning the shell.

With respect to the pole key preload case, no pole key may happen for two reasons: whether the coil pack is larger than nominal (represented in the second figure) or the pole key is smaller. Large pole key may happen for a similar but opposite reason (larger pole key represented in the third image).

When comparing no pole key to the pole key case, the coil being larger, the coil to collar contact happens earlier. This can be seen in the shell key plot as a shift to the left, i.e. smaller key size for a given stress. From the pole point of view, a similar shift takes place. However, in the no pole key case, the coil receives all the compression. Thus, the slope is larger and, consequently, the shell target stress can be reduced (figure 15).

When comparing large pole key to pole key case, the contact from the shell point of view should also happen earlier. However, from the pole point of view, there would not be a contact at that point which is why the pole key plot is shifted slightly right compared to the shell in figure 15. Now, the shell target stress needs to be higher compared to that in the no pole key case as part of the stress is intercepted by the key.

6.3. Coil pack size, theoretical load key and contact keys

For a constant load key thickness, a larger coil pack leads to increased azimuthal preload. The condition for a constant

Table 1. MQXFB preload characterization and comparison to short models.

Magnet	$\Delta R_{\mathrm{coilpack}}$	g_{pk}	$\sigma_{\theta,\mathrm{s}}$	$\sigma_{\theta,\mathrm{p}}$	F_{rod}	k_{s}	k_{p}	k_{TF}	t_{s}	t_{p}	t_{d}	σ_{o}	$\Delta R_{\mathrm{coilpack,s}}$	$\Delta R_{\mathrm{coilpack}}$ diff
MQXFS3a	−105	−50	84	−75	0.23	124	−99	−0.8	13.15	13.25	−100	10	−150	−45
MQXFS5	−111	50	104	−101	0.58	128	−152	−1.2	13.22	13.25	−30	5	−220	−109
MQXFS3c	−136	200	101	−116	0.69	122	−163	−1.3	13.3	13.36	−60	10	−300	−164
MQXFS4	−264	100	59	−76	0.67	123	−205	−1.7	13.38	13.41	−30	6	−380	−116
MQXFS6a	−118	300	67	−83	0.72	112	−134	−1.2	13.11	13.11	0	0	−110	8
MQXFS6b	−102	npk	64	−93	0.67	128	−209	−1.6	13.34	13.38	−40	8	−340	−238
MQXFBP1 LE	−81	300	66	−92	0.60	107	−158	−1.5	13.19	13.22	−30	5	−190	−109
MQXFBP1 CE	9	350	85	−101	0.60	112	−165	−1.5	13.04	13.20	−160	26	−40	−49
MQXFBP1 RE	−86	280	65	−89	0.60	93	−151	−1.5	13.11	13.22	−110	17	−110	−24
MQXFBMT2 LE	−75	303	73	−106	0.50	129	−186	−1.4	13.18	13.23	−50	9	−180	−105
MQXFBMT2 CE	−19	335	82	−102	0.50	135	−143	−1.2	13.13	13.09	40	−6	−130	−111
MQXFBMT2 RE	−87	261	73	−100	0.50	127	−163	−1.3	13.19	13.21	−20	3	−190	−103
MQXFBP2 LE	−179	277	36	−66	0.20	127	−207	−1.6	13.27	13.32	−50	10	−270	−91
MQXFBP2 CE	−116	289	41	−53	0.20	113	−176	−1.6	13.17	13.24	−70	12	−170	−54
MQXFBP2 RE	−189	241	33	−47	0.20	126	−181	−1.4	13.28	13.28	0	0	−280	−91
MQXFBP2 LE 2	−179	277	54	−100	0.45	97	−168	−1.7	13.22	13.21	10	−2	−220	−41
MQXFBP2 CE 2	−116	289	58	−82	0.45	97	−135	−1.4	13.17	13.20	−30	4	−170	−54
MQXFBP2 RE 2	−189	241	50	−77	0.45	104	−158	−1.5	13.28	13.31	−30	5	−280	−91
MQXFB01 LE	−183	235	46	−77	0.47	104	−148	−1.4	13.23	13.15	80	−12	−230	−47
MQXFB01 CE	−146	270	50	−84	0.47	111	−149	−1.3	13.19	13.12	70	−10	−190	−44
MQXFB01 RE	−168	248	42	−66	0.47	103	−124	−1.2	13.24	13.18	60	−7	−240	−72
MQXFS AVG	−139	120	80	−91	0.59	123	−160	−1.30	13.25	13.29	−43	6	−250	−101
MQXFB AVG LE	−130	279	66	−92	0.44	117	−175	−1.48	13.22	13.23	−13	3	−218	−88
MQXFB AVG CE	−68	311	85	−101	0.44	118	−158	−1.39	13.13	13.16	−30	6	−133	−64
MQXFB AVG RE	−133	258	65	−89	0.44	112	−155	−1.39	13.21	13.22	−18	3	−205	−72

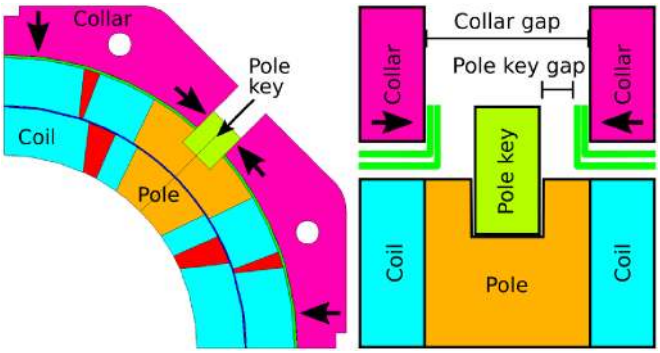

Figure 14. Collar gap geometry and topology views, respectively. The large arrows illustrate the displacement direction in azimuthal preload: collars are pushed toward the center of the magnet that reduces the collar gap.

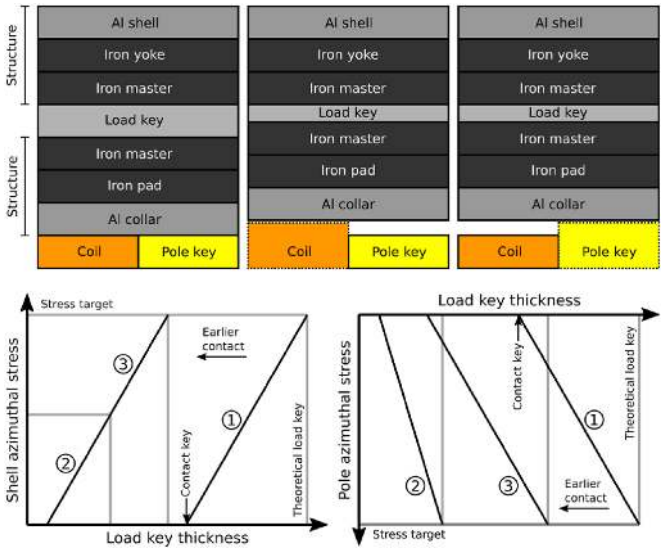

Figure 15. The top image shows the MQXF mechanical topology from azimuthal loading point of view in three cases: (1) pole key, (2) no pole key and (3) large pole key. The bottom image shows a schematic view of the shell and pole key plots in the different cases.

azimuthal preload in MQXF without a pole key to collar contact can be formulated as

$$\Delta t_{\text{load}}(z) + \Delta R_{\text{coilpack}}(z) + \Delta t_{\text{structure}}(z) = 0 \tag{4}$$

where Δ means the difference w.r.t. nominal value, t_{load} is the nominal load key thickness and $t_{\text{structure}}$ is the nominal structure thickness. The structure thickness is an implicit definition of a value that is composed of all the rest of the mechanical parts taking part in the stress transfer in loaded states (figure 15). Also, as seen in equation (4), only the deviation from the nominal thickness is of interest. Let us define the theoretical load key as a load key that assures a constant azimuthal stress over the length of the magnet. Thus, by assuming a constant structure variation $\Delta t_{\text{structure}}$, the theoretical load key variation over the length for inducing a constant azimuthal preload can be easily calculated with equation (4) and depends only on the coil pack size variation.

It is shown in [12] that the azimuthal preload can be expressed as a function of the load key thickness (key plots in figure 15)

$$\sigma_\theta(z) = k t_{\text{load}}(z) + \sigma_{\theta,0}(z) \tag{5}$$

where σ_θ is the azimuthal stress, k is the slope and $\sigma_{\theta,0}(z)$ is a fitting constant that can be used to determine the size of the contact key (figure 15)

$$t_{\text{contact}}(z) = \sigma_{\theta,0}(z)/k \tag{6}$$

that is the load key that enforces a contact between the structure and the coil pack before inducing any stress. The size is at the intersection of the load key size axis and the key plot line. There are two flavors of these formulations: the shell and the pole. The variables are distinguished by adding the flavor to its name and subscripts s and p to its symbol, respectively. For example, the shell slope is k_{s} and the pole slope is k_{p}. The contact keys for shell and pole can also be noted simply as t_{s} and t_{p}, respectively.

The key plot function in equation (5) can be expressed in a different form using the contact key equation (6)

$$\sigma_\theta(z) = k(t_{\text{load}}(z) - t_{\text{contact}}(z)) = k t_{\text{if}}(z), \tag{7}$$

where $t_{\text{if}} = t_{\text{load}} - t_{\text{contact}}$ is the load key interference. This means that the stress induced by the theoretical load key is offset by the contact key. Moreover, the definition of the theoretical load key requires that the stress over the length must be constant. Thus, equation (7) yields a relationship between the variation of contact key and the theoretical load key

$$\frac{\mathrm{d}t_{\text{if}}(z)}{\mathrm{d}z} = 0 \Leftrightarrow \Delta t_{\text{load}}(z) = \Delta t_{\text{contact}}(z). \tag{8}$$

The theoretical load key variation and the contact key variation are interchangeable in all the equations above. This means, in the light of equation (4), that a smaller coil pack or structure leads to a larger theoretical load key that requires a larger contact key that implies later contact and that the coil pack size can be determined from the contact key

$$\Delta R_{\text{coilpack}}(z) = -\Delta t_{\text{contact}}(z) - \Delta t_{\text{structure}}. \tag{9}$$

The coil pack size can be determined with both contact key flavors. However, the pole contact key is less reliable due to the possibility of coil bending (section 6.7). Thus, only the shell contact key is recommended. The contact keys and coil pack sizes (based on shell contact keys and shimming plans) in table 1 show that the coil pack size, based on shell contact key ($R_{\text{coilpack,s}}$), is always smaller than the coil pack size based on the plan (R_{coilpack}). The average difference (R_{coilpack} diff) is -101 μm in short models; -88, -64 and -72 μm (LE, CE and RE) in long magnets. In equation (9) this is formally explained by $\Delta t_{\text{structure}}$. However, it is also possible that the coil size changes during loading. In this work the convention of 100 μm smaller structure is used in the FE models.

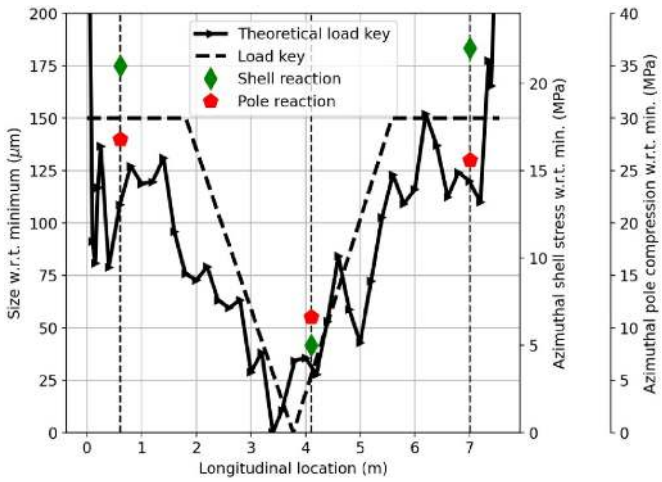

Figure 16. MQXFBMT2 theoretical load key, used variable load key profile, measured shell reaction and measured pole reaction. The left vertical axis shows the size that is measured with respect to the smallest thickness of the key over the length. The shell and pole reactions to such a key is shown on the right vertical axis, respectively. Again, the reactions are relative to the smallest reaction over the length.

6.4. The variable load key method

From equations (1) and (4) it follows that in principle one could vary the MP or radial shimming along the length in order to achieve equivalent effect as with the variable key size method or one could vary the structure thickness which would mean changing the sizes of loading pads or some other mechanical parts. The advantage of variable shimming is that each coil could be optimized individually over its length. However, changing the load key is the most practical solution. Moreover, one could decide to correct the loading conditions over the length after the magnet is already loaded by simply replacing the keys with the variable load key, taking into account the feedback from the strain measurements.

The preload characterization in [12] shows that the $\Delta t_{\text{structure}}$ in the short models is on average -101 μm (slightly less in long magnets as seen in table 1) which indicates a smaller coil pack than in reality or a smaller structure. The shell slope on average is around 120 MPa mm^{-1}. The pole slope for a no pole key and pole key cases are around -200 and -100 MPa mm^{-1}, respectively. How much stress does the theoretical load key induce along the length? If the stress variation due to the structure is assumed zero, equations (4) and (7) yield

$$\Delta\sigma_\theta(z) = -k\Delta R_{\text{coilpack}}(z). \tag{10}$$

The no pole key case theoretical load key size is plotted in the last figure column in figure 10 for all the MQXFB coil pack assemblies considered in this work. The plot shows also its effect on tension and compression variation over the length according to equation (10). The values are w.r.t. the minimum for shell and pole

For example, MQXFBMT2 theoretical load key plot shows that a key 125 μm larger at the ends compared to the center would equalize the stress over the length. Generally, a 150 μm larger key increases the shell stress by 18 MPa. The increase on the pole would be 30 MPa in a no pole key case (represented in the plot) and 15 MPa in a pole key case. Figure 16 shows the theoretical load key used in MQXFBMT2 (no pole key) mechanical test and the measured shell/pole reaction. The theoretical load key at LE is about 110 μm larger than its smallest thickness (located at around 3.3 m) whereas the actual load key is 150 μm larger than its smallest (located at around 3.7 m). The measured reactions at the LE in the shell and pole are about 21 and 28 MPa. Based on the load key, the expected values are 18 and 30 MPa. The reactions are relative to the previous key (the key size did not change in the middle when variable key was used). The center gauge is not exactly at the center. Therefore, some stress is generated. The results show that by using a variable load key, it is possible to correct stress variation along the length.

If a constant key thickness is used, the stress variation along the length with respect to the maximum is the opposite of the stress induced by the theoretical load key. For example, in MQXFBMT2 the shell stress would be 18 MPa less at the ends compared to the center, 30 and 15 MPa on the pole in no pole key and pole key cases, respectively.

6.5. The transfer function and the role of the pole key

The mechanical development of MQXF magnets started with successful tests of the support structures for short models (MQXFS) housing dummy coils [4, 5, 22]. The studies hinted at the critical role of the pole key in the azimuthal preload. The pole key is to provide azimuthal alignment between the coils and the structure without contributing to the preload [5]. However, as seen through the topological illustration and key plots in section 6.2, the pole key may intercept a part of the stress and thus make the transfer from the shell to the coils less effective. In [22] the simulated and measured pole strain vs shell strain transfer function (TF) curves show that there is a great difference in between the functions of a structure with or without the pole key. In [23] the so called TF (pole stress vs shell stress) for MQXF was introduced. The role of the pole key was analyzed using an ANSYS model and three different dummy assemblies. The first short model (MQXFS1) housing the actual superconducting coils was also preloaded and the first reference ANSYS 2D model of MQXF was optimized using measured strain data of real coils. The short models MQXFS1/S3/S5 were tested and the mechanical analysis focusing on variation of stress by means of pole key shimming and load key thickness were discussed in [24]. In [10] it is shown that shell stress varying from 120 to 180 MPa yields roughly a constant nominal pole stress of around -120 MPa due to the varying influence of pole key.

Based on the key plots, the TF can be formulated as follows

$$\sigma_{\theta,\text{p}}(\sigma_{\theta,\text{s}}) = k_{\text{TF}}\sigma_{\theta,\text{s}} + \sigma_{\text{o}}, \tag{11}$$

where the slope can be written with the help of the shell and pole slopes

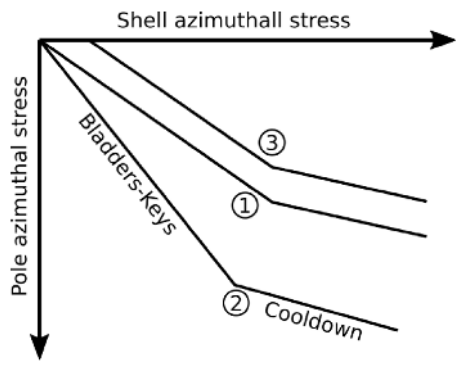

Figure 17. The TF of MQXF in the three cases shown in figure 15: (1) pole key case $\Rightarrow k_{\mathrm{TF}} \approx -0.8$, (2) no pole key case $\Rightarrow k_{\mathrm{TF}} \approx -1.7$ and (3) large pole key case $\Rightarrow k_{\mathrm{TF}} \approx -0.8, \theta_{\mathrm{o}} > 0$. In addition to the bladder-key operation the MQXF also incorporates preload gains through cooldown that is also presented in the TF.

$$k_{\mathrm{TF}} = \frac{\mathrm{d}\sigma_{\theta,\mathrm{p}}}{\mathrm{d}\sigma_{\theta,\mathrm{s}}} = \frac{k_{\mathrm{p}}}{k_{\mathrm{s}}}. \tag{12}$$

The shell slopes do not usually change much, see table 1 and [10]. The shell slopes are on average 123 and 112–118 MPa mm^{-1} for short and long magnets (smaller value in long magnets is not understood). FE model shows that the shell slope should be 120 MPa mm^{-1}.

Therefore, the TF slope is dictated by the pole slope: in the pole key case the pole slope is more gentle than in the no pole key case and that is the case also in the TF. The pole stress at zero shell stress, called the pole offset, can be written with the help of pole flavor of equation (7) as

$$\sigma_{\mathrm{o}} = k_{\mathrm{p}}(t_{\mathrm{s}} - t_{\mathrm{p}}). \tag{13}$$

This is just the pole stress at the shell contact key. In the case of a large pole key, the contact happens earlier on the shell side than on the coil side. Thus, according to equation (13), $t_{\mathrm{s}} < t_{\mathrm{p}} \Rightarrow \sigma_{\mathrm{o}} > 0$ implies a positive vertical shift in the TF (note that $k_{\mathrm{p}} < 0$). An example of the shift is observed in MQXFS3a (see figure 3 in [12]) with $\sigma_{\mathrm{o}} = 10$ MPa (table 1). The pole offset is not necessarily physical: if the contact is seen on the shell before the pole, there cannot be any stress on the pole even if the pole offset indicates tension.

It can be concluded that there are roughly three main cases of MQXF preload that are mentioned earlier in section 6.2 and plotted in terms of pole key plots in figure 15. The nature of these cases can be described with the help of the TF slope and the pole offset: (1) gentle slope (-100 MPa mm^{-1}/120 MPa mm^{-1} ≈ -0.8 MPa MPa^{-1}), (2) steep slope (-200 MPa mm^{-1}/120 MPa mm^{-1} ≈ -1.7 MPa MPa^{-1}), (3) gentle slope with a positive vertical pole offset. The cases are shown in figure 17 in terms of TF. The cool-down has a significant effect on the preload as the aluminum shell shrinks more than the coil. This is illustrated as the second linear part in figure 17.

6.6. The collar gap and the pole key gap

One of the critical design parameters has historically been the pole key gap [24] that is the free distance between the pole key and the collar (assuming the pole key is in the middle of the collar gap) and denoted with g_{pk} (table 1). In addition to the pole key, two layers of 125 μm GI are added on the collars that further reduce the gap. The nominal size of the collar gap is 15 mm and the pole key is 13.9 mm wide, thus the nominal pole key gap is 300 μm.

As seen in section 6.5, the pole key may intercept a part of the compression intended for the coil if the pole key is in contact with the collars. This happens if the pole key gap is not large enough (MQXFS3a). The pole key to collar contact may happen also later during the azimuthal preload or during cool-down as the azimuthal displacement tends to close the gap. Moreover, the contact may be one sided as the coil azimuthal excess can be asymmetric and the shimming convention is symmetric [10].

The condition for a well coupled coil to collar interface is that the quadrant sector at the outer radius of the coil pack and the inner radius of the collar must be of equal lengths (figure 7) and in particular any deviation from the nominal in the coil pack outer radius leads to an equal deviation on the collar side

$$c_{\mathrm{collar}} = c_{\mathrm{coilpack}} \Leftrightarrow \Delta c_{\mathrm{collar}} = \Delta c_{\mathrm{coilpack}}, \tag{14}$$

where c_{collar} and c_{coilpack} are the collar and coil pack azimuthal average quadrant lengths (1/4th of the total circumference) along their curvatures at the contact interface. According to figures 7, 14 and equation (14), assuming nominal collar sizes, the variation on the collar side in a well coupled situation depends on the coil pack size

$$\Delta g_{\mathrm{collar}} = \Delta c_{\mathrm{coilpack}} = \pi \Delta R_{\mathrm{coilpack}}/2, \tag{15}$$

where g_{collar} is the collar gap. The contact gap, i.e. the distance from coil pack to collar, can be defined as

$$g_{\mathrm{contact}} = 2\,\Delta g_{\mathrm{collar}}/\pi - \Delta R_{\mathrm{coilpack}}. \tag{16}$$

If the coil and collar are well coupled, i.e. equation (15) holds, then $g_{\mathrm{contact}} = 0$. Moreover, the pole key gap depends on the collar gap and its variation is

$$\Delta g_{\mathrm{pk}} = \Delta g_{\mathrm{collar}}/2, \tag{17}$$

where g_{pk} is the pole key gap.

Figure 18 top plot shows the measured collar gap variation over the length and the coil pack sector length computed along the length with equation (15) for MQXFBP1. The bottom plot shows the correlation between the first and second terms of right side of equation (16), i.e. the collar radius and the coil pack size variations, respectively. The collar gap measurements are taken at the pad bolting locations with a caliper. Each measurement point (along the length) is an average of the

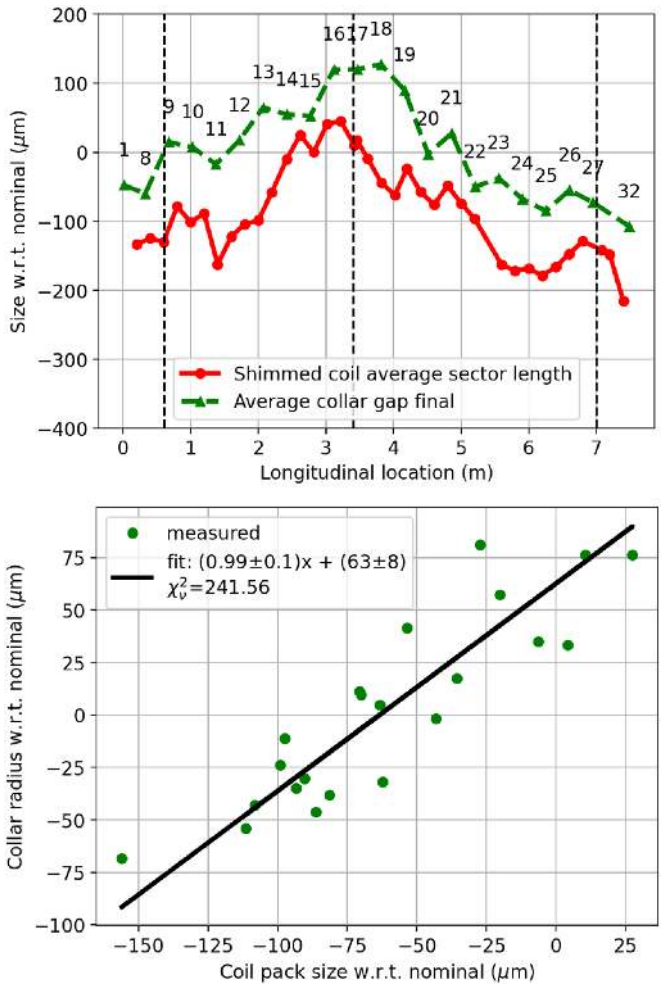

Figure 18. Top plot: the coil average sector length variation and the collar gap variations along the length, bottom plot: the correlation between the collar radius variation and coil pack size. Bolt numbers are written over the collar gap measurement curve at each bolt location where the measurement is taken. There are 32 bolts in total, bolts 2–7 and 29–31 are are tightened but not measured.

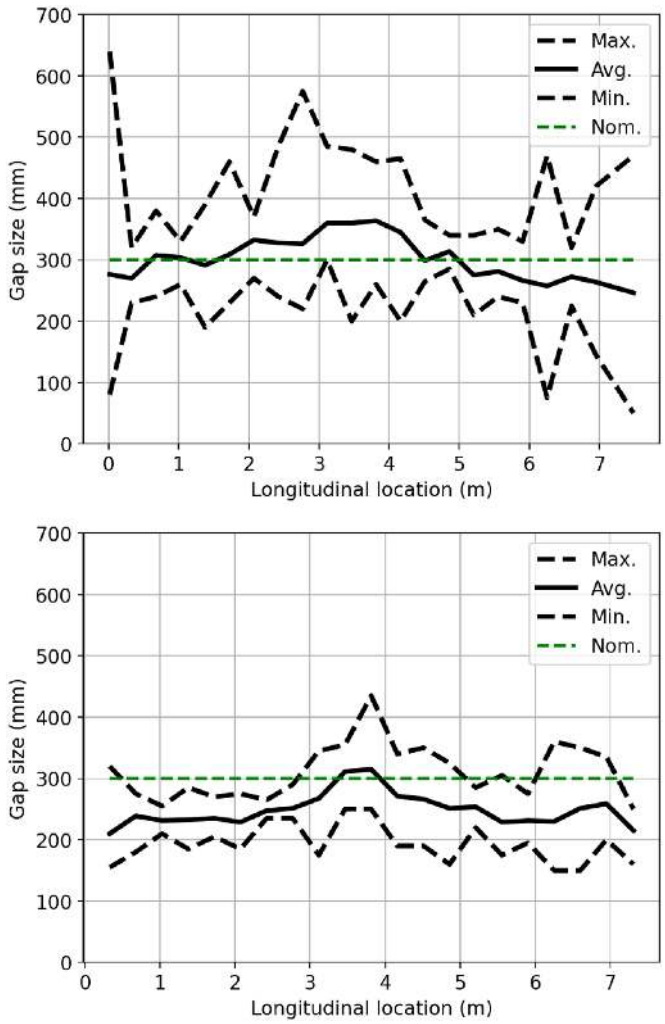

Figure 19. The pole key gap along the length in MQXFBP1 (top) and MQXFB01 (bottom).

four collar gap readings (figure 4). The slope indicates the collar gap variation is sensitive to the coil pack average size. The positive offset means that on average there is a gap between the collar and the coil, which means that the coupling is sub-optimal. However, the average contact gap (offset) is small, for example only 63 μm in MQXFBP1. This gap is also seen in the FUJI paper imprints (see example in figure 6) where the contact is not uniformly represented.

Figure 19 plot shows the pole key gap variation along the length as defined in equation (17). The average pole key gap is close to nominal (300 μm), larger at the center and smaller at the ends as predicted by the coil sizes. The maximum and minimum curves show that in the bolting phase, there can be some imbalance between the collar gaps. The bolt tightening follows a procedure where the bolts are tightened first using 10 Nm torque and then 20 Nm torque. In each section, at a longitudinal position, the tightening is always performed to diametrically opposed pairs (two tightening operations per section). The sections are tightened starting from the center toward the extremities of the magnet. In MQXFB01, special tuning of the bolts (tightening one and loosening another) was added on top of the formal procedure. The effect can be seen in the decreased pole key gap imbalance (max–min). One can also see the overall smaller pole key gap due to smaller coil pack in MQXFB01 (CE w.r.t. nominal, 9 μm vs -75 μm, table 1).

6.7. The LQ effect on MQXF

After bolting, the collar gap measurements show that there is a contact gap about 50–100 μm between coil and collar. Additionally, the experience with FUJI test imprints indicates that the contact is not uniform and it is usually more represented at the pole. This is also consistent with the cross-section metrology views in figure 9: the pole is usually extended compared to the MPs.

In [12] a preload characterization technique of MQXF was introduced. The TF analysis together with the shell and pole key plots was used to develop the theory for analyzing the MQXF preload in detail. The theory focuses on the role of the

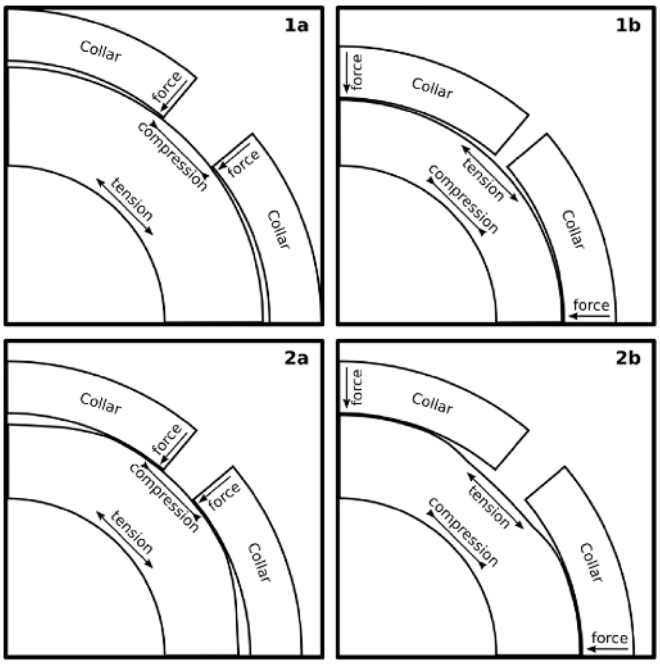

Figure 20. Four cases of coil to collar non-conformity: (1a) coil pack is large, (1b) coil pack is small, (2a) pole bump (or MP dent), (2b) pole dent (or MP bump).

load key size, coil size and in particular the coil-collar non-conformities. The theory led to the method of variable loading key technique to coils whose size are smaller at the extremities than at the center. Moreover, with the help of the new preload analysis a systematic error in MQXFB coil metrology procedure was found. The error made the coils appear smaller than in reality due to a reference geometry that was 125 μm too large per MP.

All short model magnets produced and tested at CERN were analyzed and the so called LQ effect on MQXF, that justifies the convention [11] of removing 125 μm compared to the theoretical radial shimming, was explained. In essence, the LQ effect was originally bending of the pole due to too big coils (observed first in the LQS01 magnet [11], hence the name). The preload theory [12] expanded on this notion exemplifying that a too big/small coil with a deviation in the order of 125 μm (or a bump/dent deviating in the order of 50 μm on the coil nominal outer curvature) may cause bending with a detectable shift in the TF and key plots. From the principle of induction, it follows that a non-conforming coil to collar interface might cause bending on the pole.

Based on the LQ effect study, four pure (as opposed to mixed) cases of coil to collar non-conformities are shown in figure 20. The first category is the variation of radial size: a coil pack quadrant can be too (1a) large or (1b) too small radially. In these cases, the collars touch only on the poles or on the MPs and as the azimuthal prestress increases, the coil is forced to seek a conforming shape that leads to bending, i.e. tension or compression on the pole inner surface (where the pole stress is measured), respectively. The second category is the variation of shape: a coil pack quadrant may have a (2a) bump on the pole (or dent near the MP) or (2b) dent on the pole (or bump near the MP). The effects due to (2a) and (2b) are similar to (1a) and (1b) with similar explanations. Let us call the different pure cases: (1a) large coil, (1b) small coil, (2a) pole bump (or MP dent) and (2b) pole dent (or MP bump).

Table 2. Coil to collar non-conformity effect pure case comparison.

Case	t_s	t_p	t_d	σ_o
Large coil	↓	↓↑	↑	↑
Small coil	↑	↑↓	↓	↓
Pole bump (MP dent)		↑	↑	↑
Pole dent (MP bump)		↓	↓	↓

If the coil pack is too large or small it is seen on both contact keys that are smaller or bigger than nominal, respectively. Additionally, there will be pole offset in the TF due to tension (upwards shift) or compression (downwards shift) on the pole inner surface. According to equation (13) there has to be an additional shift of

$$t_d = -\sigma_o/k_p, \tag{18}$$

in the pole key plot, where t_d is the contact key difference. Thus, for a large or small coil pack (pole tension or compression), contact key decreases or increases w.r.t. shell contact key.

Table 2 shows the effects of the aforementioned four pure cases of non-conformity. The double arrows mean that on one hand the contact key may increase or decrease but on the other hand it may do the opposite. For example, increased coil size decreases the contact key but at the same time it increases via tension due to bending. The pure cases can be mixed, in particular when fixing a nonconform shape, e.g. a pole bump + small coil pack. It is trivial to correct a large or a small coil pack. However, from the pole bending point of view the table shows that pole bump or dent can be corrected in a similar way, by removing or adding radial shims, respectively. In general, there can be many shapes that cause tension or compression on the pole inner surface. The current theory would classify these as pole bump-like or pole dent-like shapes, respectively (also MP dent-like or MP bump-like). For example, following this classification, a large coil would be a pole bump-like shape.

In [12] these effects are demonstrated with an FE model and presented in a TF and key plot form. In the shell key plot graphs, one may notice that the MP bump and dent have a small effect on the contact keys. This is because the theory assumes a linear slope, whereas in reality there is a contact regime (seen also in the aforementioned plots). Within this regime, where the behavior is non-linear, the coil pack under stress adapts into a deformed shape. The contact keys are defined in a range of loaded states. Therefore, the determined coil pack size adopts the deformed shape. Moreover, from a theoretical point of view, a coil with a nonconform coil pack to collar contact is of nominal size if the shell contact key size is that of a nominal coil pack. Therefore, one could also say that the so called pure cases in [12] are close but not exactly pure as their size is not nominal which is logical as material is removed or added with respect to nominal (despite the nominal curvature outside the location of removal).

7. The role of the stainless steel shell

The MQXF is housed inside a stainless steel shell (SS shell, also LHe SS vessel, figure 1). In practice, it consists of two halves that are welded together on both sides of the magnet in order to form and install the full shell on top of the aluminum shell. So far the SS shell has been tested once in the first short model (MQXFS1) with 100 MPa pretension [25, 26] and the tests did not show any signs of issues. The shell will present in all the MQXFB magnets.

It is possible to adjust the azimuthal stress of the SS shell by changing the circumference of it. Thus, the process may have an effect on the state of the preload. However, the purpose of the SS shell in the nominal design is to merely contain the magnet and the liquid helium (cooling medium) without a contribution to the preload. Thus, one should take into account that when the magnet is cooled down, the aluminum shell shrinks more than the SS shell. Therefore, some azimuthal tension on the SS shell is needed after the shell welding so that it has no (or very little) stress after cool down but is in contact with the aluminum shell.

One of the downsides is that the shell strain gauges need to be removed before this operation. However, the pole strain can be monitored and it shows if the SS shell has an effect on the preload. In MQXFBP1 the SS shell was also equipped with strain gauges before the process. The gauges were placed on the inside and outside surfaces of the SS shell for assessing the average azimuthal stress. The installation of inner gauges is possible due to the aluminum shell cutouts at the extremities of each shell. Azimuthally, the locations are at the yoke cutouts (figure 1), for example close to but less than 45° for Q1 (symmetrically for all quadrants). The average stress is computed using the inner and outer gauge at each location.

There is a certain probability of loosing a strain gauge and when installing them in challenging locations (like in the cutouts) this probability increases. Additionally, if one gauge is lost then so is the measurement at that location. Thus, the probability of loosing a measurement location that depends on two gauges is twice as that of one gauge. In MQXFBP1, 7 out of 12 locations were lost. It is recommended that in the future the gauges are backed up by another set of gauges.

The strain is measured before and after the shell welding process. Figure 21 shows the measured and computed stainless steel shell stress as a function of change in azimuthal pole stress in MQXFBP1. The computation is done with the 2D ANSYS octant model. During cool down, 80 MPa is lost in the SS vessel that makes 15 MPa (NPK) on the pole. Thus, if the stress change is more than −15 MPa then the SS shell is still in contact with the aluminum shell, otherwise not. In MQXFBP1, the SS shell stress at room temperature was aimed at 50 to 150 MPa for an effect of −17 to −8 MPa that after the cool down would be −2 to 0 MPa (with an Al shell to SS shell contact gap of 32 μm). LE and CE seem to agree with the PK case where as the RE agrees with the NPK case. The effect of shell welding was slightly higher than the target. This is due to too large welding gap between the SS shell hemispheres (makes the circumference smaller). The measured effect with FEM prediction is shown in table 3.

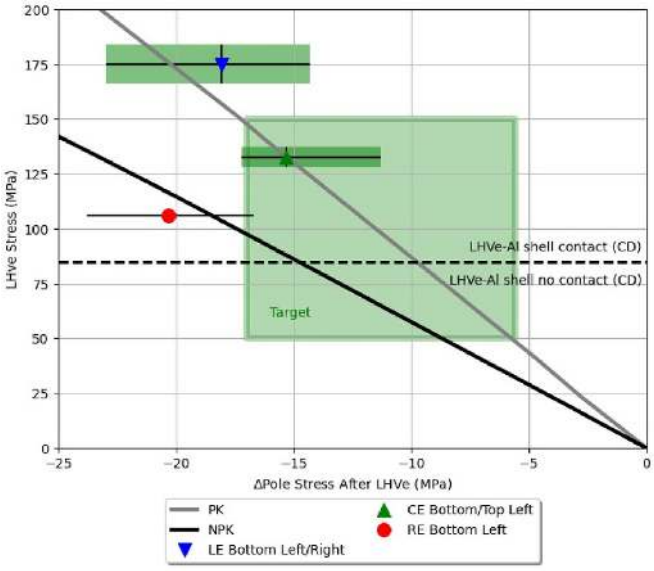

Figure 21. Stainless steel shell average azimuthal stress as a function of change in azimuthal pole stress. The horizontal dashed line shows the shell stress at which the effect on the pole is zero after cool down. The black and gray solid lines are the 2D FEM computations without and with pole key contact. Blue upper triangle, green lower triangle and red circle represent LE, CE and RE measurements. Each measurement has min/max values represented by black bars and green rectangles. The green rectangle in the middle represents the welding target.

Table 3. The effect of SS shell expected on the MQXFBP1 pole azimuthal preload based on room temperature measurements and FEM predictions.

Case	LE (MPa)	CE (MPa)	RE (MPa)	Mean (MPa)
Pole RT	−20	−15	−18	−18
Pole CD	−3	0	−1	−1

8. Cold mechanics

At cold, MQXFBP1 had strain gauges working reliably on two rods (B and C) and on the SS shell gauges. Rod A gauge signal had been lost completely and Rod D had been lost but fixed by means of quarter bridge reconfiguration (not reliable in varying magnetic fields). The strain gauges on the aluminum shell had to be removed due to the SS shell installation and all the coil strain sensor signals were lost during cool down. Thus, the acquired data is very limited.

The SGs showed that there was no effect on the SS shell during powering. The change during ramp up was in the order of 10 μe. The coil FBGs were not functional at cold, however, after a thermal cycle they showed mainly consistent results.

Figure 22 shows the rod relative (Δ) behavior during powering. The difference between FEM and measurements is roughly 2.5 fold. In a FEM study [24], a change of friction coefficient of coil to collar surface from 0.16 to 0.13 led to a change in delta rod stress from 4.4 to 6.9 MPa. Changing the friction coefficient here between 0.2 and 0.3 does not seem to lead to a large change in delta rod stress compared to [14]. The

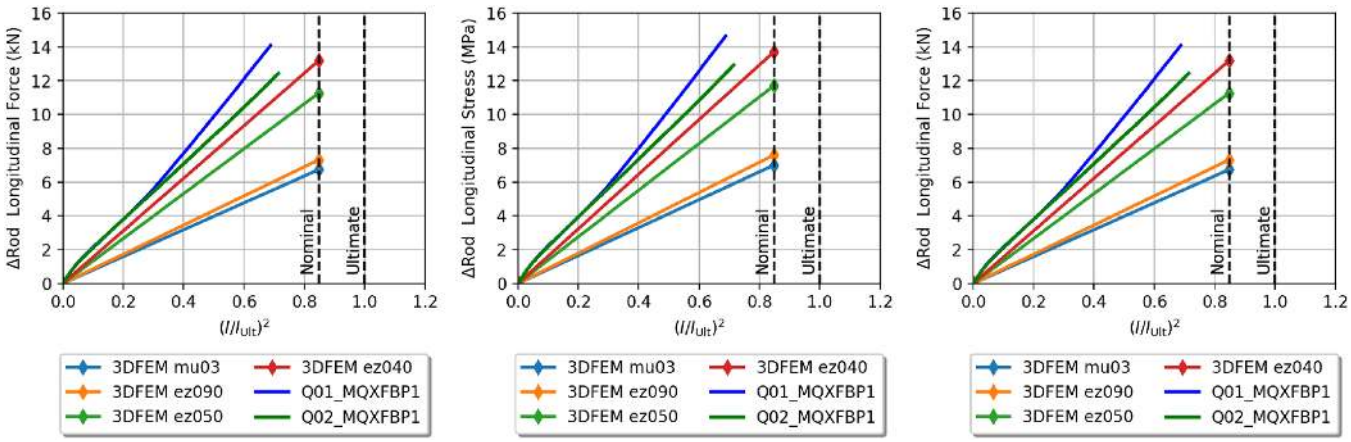

Figure 22. Rods vs normalized current squared: comparison of the measured values and computed values. 3D FE models are computed with 0.3 friction and varying axial elastic modulus using orthotropic yoke material approximation. The rod force at nominal current is 1.17 MN; large portion of it is held by the friction.

Table 4. Rod comparison of different MQXF magnets at nominal current. Thin and thick refer to the lamination type. MQXFB values are extrapolated.

Magnet type	$\Delta\varepsilon$ (μe)	$\Delta\sigma$ (MPa)	ΔF_{rod} (kN)	$\Delta F_{\mathrm{axial}}$ (kN)	$\Delta F_{\mathrm{axial}}/F_{\mathrm{em,nom}}$ (%)	Δl (μm)
MQXFS thick	56	4.4	4.5	18	1.5	84
MQXFS thin	85	6.7	6.8	27	2.3	127
MQXFA	64	14	13	52	4.4	290
MQXFB	79	17	16	64	5.5	590

coefficient cannot be lowered toward zero due to numerical instabilities. Moreover, a coefficient of 0.16 seems already low (laminated aluminum, polyimide surface). Instead, a variation of the axial elastic modulus in orthotropic approximation was tried for the laminated yoke. The modulus had to be lowered down to 40% (90 GPa) of the original in order to match the measured values. Table 4 shows a comparison with the short model magnets and the MQXFA (4.5 m long magnet type). The MQXFS have different elongations during ramp depending on the lamination type used in the structure that could be due to increased packing errors when going from thick to thin laminates. This supports the idea of a lower axial modulus.

Figure 22 shows a distinct change of slope at $0.3(I/I_{\mathrm{Ult}})^2$ and the difference in absolute strain before/after the current ramp is about 20 μe between first and second powering. This means that the irreversible elongation is about 150 μm during the first ramp.

Table 5 shows the effect of cool down on the SS shell strain. The measured delta in cool down and warm up was, respectively, 14% larger and 10% smaller, compared to the expected value (2D octant FEM).

Figure 23 shows the SS shell movement at the end of MQXFB at different phases of a thermal cycle according to 3D FEM computation. Longitudinally, the SS shell is made of one continuous piece, whereas the Al shell is segmented. Thus, the stainless steel shell shrinks more than the rest of the structure. Figure 24 shows that the friction coefficient has a significant role on the movement. After cool down, the SS shell might not return to its original position. This effect was observed in MQXFBP1 with a 3 mm shift. The 3D FEM cannot reproduce this even with a friction coefficient of 0.1 giving the highest shift of about 2 mm. It is possible that the welding process has a contribution on it.

Table 5. The effect of cool down on the MQXFBP1 SS shell average strain ($\varepsilon_{\mathrm{avg}}$). Δ denotes the change w.r.t. the previous step and $\varepsilon_{\mathrm{FEM}}$ is strain predicted by the FEM.

Step	$\varepsilon_{\mathrm{avg}}$ (μe)	$\Delta\varepsilon_{\mathrm{avg}}$ (μe)	$\Delta\varepsilon_{\mathrm{FEM}}$ (μe)
Warm	459	0	0
Cool down	10	−449	−381
Warm up	363	353	333

9. Discussion

The joint effort of HL-LHC and AUP projects producing MQXF magnets is in preseries production. From CERN side the MQXFBP1 (prototype) has been assembled, tested and disassembled. The MQXFBP2 (prototype) and MQXFB01 (preseries) have been assembled and preloaded. Moreover, six short model magnets have seen their full lifecycles that have helped immensely in the development of the mechanical theory of MQXF.

The measured coil sizes were taken into account in the full FE model. In modeling, the convention of assuming a 100 μm smaller structure, as reported in earlier studies, is used resulting in a good agreement with the measured shell keyplot data.

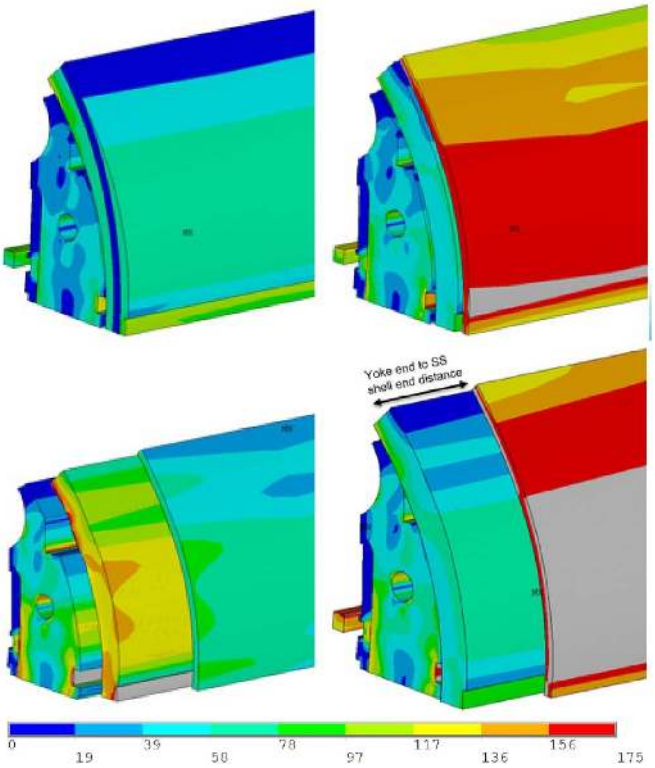

Figure 23. Stainless steel shell movement according to 3D FEM: without ss shell, after shell welding, after cool down and after warm up. The displacement is scaled with a factor of 50 and the color map is Von Mises stress from 0 to 175 MPa.

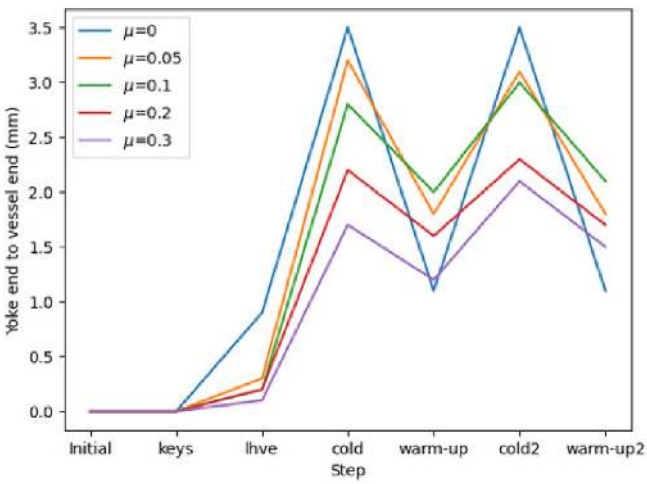

Figure 24. Stainless steel shell movement due to thermo-cycles with different friction coefficients between the Al and SS shells according to 3D FEM.

The FEM results are well in line with the prototype showing a slight LQ effect. However, the LQ effect is not enough for explaining the large pole offset at the center.

Jumps were observed in some of the MQXFBP1 FBG strain values during preload which led to difficulties in regards with interpreting the data. A mechanical test equipped with strain gauges and FBGs at the same location confirmed that the FBGs do not always correspond to the coil strain due to unexplained shifts with respect to electrical strain gauge readings. Nevertheless, as the sensitivity of the fiber was proven to stay intact, one can simply remove the shifts assuming the exact temporal location is known, as was done in MQXFBP1 preload characterization.

The recent theory development in the preload characterization helped to reveal a systematic error in coil metrology results that underestimated coil sizes. MQXFBP1 was originally targeted at the MQXFS4 shimming that has the lowest coil pack size. However, MQXFBP1 coil pack size ended up being the largest due to the underestimated size. Nevertheless, the size is still nominal as the MQXF magnets are conventionally shimmed 125 μm smaller than nominal due to the LQ effect.

Extensive work and theoretical effort has been put in producing a well defined, conforming and rigid coil to collar interface. Mechanically, this is the key interface where all the support structure takes part in. FUJI tests show that there is some nonconformity in the initial coil to collar interface that accounts for the 63 μm contact gap (according to collar gap measurements). Based on the FUJI imprints, poles are well represented, whereas usually the MPs suffer from missing contact. This can be the explanation for a pole bump like behavior (positive pole offset and negative contact key difference) throughout the magnets. MQXFB01 is the exception that has pole compression (the opposite) but it has also the smallest coil pack.

It was shown that full bladder operation mode is symmetry conserving whereas the quadrant mode is symmetry breaking. They both have the same threshold pressure that needs to be overcome before making more space for the next key. FEM shows that the additional space requires 500 and 150–200 bars mm^{-1} in full and quadrant modes, respectively. For example, assuming 100 μm extra space for inserting the new key in MQXFBP1, the last key requires 21 bars more in full mode. The difference increases by 320 bars mm^{-1} for more extra space.

The signals of all FBG sensors were lost during cool down in MQXFBP1. However, they recovered during warm up. The reason is most likely fiber misalignment in the vacuum feedthrough connector. During cold tests, the stainless steel shell and two rod signals were functional and reliable.

The stainless steel shell should be installed such that it does not play a role in the preload. About 80 MPa of the stress, corresponding to 15 MPa on the pole (no pole key), is lost during the cool down due to the different thermal contraction of the shell and rest of the magnet. Therefore, the shell has to be pretensioned as it should still remain in contact with the Al shell after cool down. In MQXFBP1, the shell welding induced 18 MPa additional compression. After cool down, the effect of stainless steel shell was thus 3 MPa on the pole. The average change of strain due to warmup was 6% higher than predicted (cool down 18%).

During cool down the stainless steel shell (made of one piece) contracted more longitudinally than the other structure and did not assume its original state after warm up, but got stuck to the aluminum shell. Simulations show that the difference to original depends on the friction coefficient; 0.1

giving the largest difference of about 2 mm. The observed difference was about 3 mm.

The elongation of rods during the ramp up is about 2.5 times higher than previously computed with FEM. This could be related to a different friction than previously thought, or to different longitudinal mechanical properties of the coil and structure. The rod elongation in short model experiments support the idea of lower yoke laminate axial modulus. However, according to FEM, MQXFBP1 require 40% of the original modulus that seems very low. The extrapolated elongation at nominal is 80 μe (600 μm) that is 64 kN total axial force or 5.5% of the total electromagnetic pull force that is inline with the MQXFA.

10. Conclusion

In principle, the MQXFB is ready for production in mechanical point of view. However, the authors want to stress the important role of meticulous handling of details and careful analysis at the final stage of the project in order to understand the behavior and track down mistakes, as shown in this paper.

The shell/pole slopes and contact keys are great tools for studying the stiffness and size variations of the coil pack and structure. The difference in the measured shell and pole flavors give important information on the coil pack stiffness and the conformity of the collar-coil interface that may cause pole bending.

The contact keys help to reveal discrepancies in the procedure such as a systematic error found in MQXFB in coil metrology measurements that underestimated coil sizes.

The mechanical preload analysis of MQXF shows that pole and key slopes for a no pole key case reach values up to -200 MPa mm^{-1}. Thus, even a 100 μm coil pack size variation along 7 m length can cause a 20 MPa deviation on the mechanical preload that is in the order of 20% of the allowed room temperature preload. The shape of MQXF coils made of Nb_3Sn exhibit non-negligible size variations over length (around 150 μm). These variations require a careful shim design each time a coil pack is formed.

Another great tool is the contact gap that is the average gap between coil and collar. It can provide depth in the understanding of FUJI paper contact tests. This can then be used in the analysis of LQ effect where the pole bending depends on the size of the gap.

The longitudinal size variation that causes significant stress variation can be compensated with the variable load key method. It was successfully tested on a test assembly. However, at this point, the variable load key is not seen as a mandatory requirement for the current MQXFB preload procedure as the short model experience shows a large window of tolerance in successful magnets.

The full bladder operation is symmetry conserving as it is pressure driven and do not drive the system in a symmetric displacement configuration. Thus, it should not be used for centering the coil pack. On the other hand, in theory, it tends to conserve the symmetry and should be used for preload steps. The quadrant operation can be used for centering. However, it does not guarantee a homogeneous displacement over length. The required threshold pressure in full and quadrant operation is roughly the same.

Optical fiber based strain measurement systems have proved to be challenging in the case of MQXFB due to connector alignment at cryogenic temperatures and high vacuum. However, thermal cycles show that the FBG readings are reliable over the magnet life cycle when functioning properly.

Data availability statement

The data that support the findings of this study are available upon reasonable request from the authors.

Acknowledgment

The authors thank A Milanese for the guidance and support, M Guichard for the strain measurements, G Vallone for the help with 3D reference model, the colleagues at the Large Magnet Facility (LMF) for manufacturing and SM18 test facility for testing.

ORCID iDs

E Takala https://orcid.org/0000-0003-4795-2810
S Izquierdo Bermudez https://orcid.org/0000-0003-2157-4751

References

[1] Apollinari G, Béjar Alonso I, Brüning O, Lamont M, and Rossi L 2015 High-Luminosity Large Hadron Collider (HL-LHC)—preliminary design report *Technical Report* (Geneva: World Scientific)
[2] Todesco E *et al* 2013 Design studies for the low-beta quadrupoles for the LHC luminosity upgrade *IEEE Trans. Appl. Supercond.* **23** 4002405
[3] Todesco E *et al* 2014 A first baseline for the magnets in the high luminosity LHC insertion regions *IEEE Trans. Appl. Supercond.* **24** 1–5
[4] Ferracin P *et al* 2014 Magnet design of the 150 mm aperture low-β quadrupoles for the high luminosity LHC *IEEE Trans. Appl. Supercond.* **24** 1–6
[5] Ferracin P *et al* 2016 Development of MQXF: the Nb_3Sn low-β quadrupole for the HiLumi LHC *IEEE Trans. Appl. Supercond.* **26** 1–7
[6] Todesco E *et al* 2021 The high luminosity LHC interaction region magnets towards series production *Supercond. Sci. Technol.* **34** 053001
[7] Gourlay S A *et al* 2006 Magnet R D for the US LHC accelerator research program (LARP) *IEEE Trans. Appl. Supercond.* **16** 324–7
[8] Muratore J F *et al* 2020 Test results of the first two full-length prototype quadrupole magnets for the LHC Hi-Lumi upgrade *IEEE Trans. Appl. Supercond.* **30** 1–5
[9] Ambrosio G *et al* 2021 Lessons learned from the prototypes of the MQXFA low-beta quadrupoles for HL-LHC and status of production in the US *IEEE Trans. Appl. Supercond.* **31** 1–5

[10] Takala E *et al* 2021 Mechanical comparison of short models of Nb_3Sn low-β quadrupole for the Hi-Lumi LHC *IEEE Trans. Appl. Supercond.* **31** 1–6
[11] Ferracin P *et al* 2011 Mechanical performance of the LARP Nb_3Sn quadrupole magnet LQS01 *IEEE Trans. Appl. Supercond.* **21** 1683–7
[12] Takala E *et al* 2020 Preload characterization of short models of MQXF the Nb3Sn low-β quadrupole for the Hi-Lumi LHC *IEEE Trans. Appl. Supercond.* **30** 1–6
[13] Vallone G and Ferracin P 2017 Modeling coil-pole debonding in Nb_3Sn superconducting magnets for particle accelerators *IEEE Trans. Appl. Supercond.* **27** 1–11
[14] Vallone G *et al* 2018 Mechanical design analysis of MQXFB, the 7.2-m-long low-β quadrupole for the high-luminosity LHC upgrade *IEEE Trans. Appl. Supercond.* **28** 1–5
[15] Wilson M N 1983 *Superconducting Magnets* (Oxford: Oxford University Press)
[16] Mangiarotti F J *et al* 2020 Powering performance and endurance beyond design limits of HL-LHC low-beta quadrupole magnets models *IEEE Trans. Appl. Supercond.* **31** 1–5
[17] Caspi S, Gourlay S, Hafalia R, Lietzke A, ONeill J, Taylor C and Jackson A 2001 The use of pressurized bladders for stress control of superconducting magnets *IEEE Trans. Appl. Supercond.* **11** 2272–5
[18] Bianchi L 2021 Strain measurements on MQXFBP1 superconducting magnet *Technical Report EDMS*—1851752 (CERN)
[19] Russenschuck S 2011 *Field Computation for Accelerator Magnets: Analytical and Numerical Methods for Electromagnetic Design and Optimization* (New York: Wiley)
[20] Ravaioli E 2015 CLIQ—a new quench protection technology for superconducting magnets PhD Thesis University of Twente
[21] Ferradas Troitino J *et al* 2018 Applied metrology in the production of superconducting model magnets for particle accelerators *IEEE Trans. Appl. Supercond.* **28** 1–6
[22] Juchno M *et al* 2016 Mechanical qualification of the support structure for MQXF, the Nb_3Sn low-β quadrupole for the high luminosity LHC *IEEE Trans. Appl. Supercond.* **26** 1–6
[23] Vallone G *et al* 2017 Mechanical performance of short models for MQXF, the Nb3Sn low-β quadrupole for the Hi-Lumi LHC *IEEE Trans. Appl. Supercond.* **27** 1–6
[24] Vallone G *et al* 2018 Mechanical analysis of the short model magnets for the Nb_3Sn low-β quadrupole MQXF *IEEE Trans. Appl. Supercond.* **28** 1–6
[25] Pan H *et al* 2017 Mechanical design studies of the MQXF long model quadrupole for the HiLumi LHC *IEEE Trans. Appl. Supercond.* **27** 1–5
[26] Ferracin P *et al* 2019 The HL-LHC low-β quadrupole magnet MQXF: from short models to long prototypes *IEEE Trans. Appl. Supercond.* **29** 1–9